Electron Cyclotron Resonance Heating of a High-Density Plasma

Hansen, F. Ramskov

Publication date:
1986

Document Version
Publisher's PDF, also known as Version of record

RISØ-M-2594

ELECTRON CYCLOTRON RESONANCE HEATING OF A HIGH-DENSITY PLASMA

Flemming Ramskov Hansen

Abstract. Various schemes for electron cyclotron resonance heating of tokamak plasmas with the ratio of electron plasma frequency to electron cyclotron frequency, ω_{pe}/ω_{ce}, larger than 1 on axis, are investigated. In particular, a mode conversion scheme is investigated using ordinary waves at the fundamental of the electron cyclotron frequency. These are injected obliquely from the outside of the tokamak near an optimal angle to the magnetic field lines. This method involves two mode conversions. The ordinary waves are converted into extraordinary waves near the plasma cut-off layer. The extraordinary waves are subsequently converted into electrostatic electron Bernstein waves at the upper hybrid resonance layer, and the Bernstein waves are completely absorbed close to the plasma centre. Results are presented from ray-tracing calculations in full three-dimensional geometry using the dispersion function for a hot non-relativistic plasma. Radial profiles for the power deposition and the non-inductive wave-driven current due to the Bernstein waves are calculated for realistic antenna radiation patterns with parameters corresponding to the Danish tokamak DANTE and to Princeton's PLT.

July 1986
Risø National Laboratory, DK-4000 Roskilde, Denmark

This thesis has been accepted by the Technical University of Denmark in connection with the conferment of the lic.techn. (Ph.D.) degree.

ISBN 87-550-1243-4
ISSN 0418-6435

Grafisk Service, Risø 1986

CONTENTS

	Page
PREFACE	5
1. INTRODUCTION	7
2. ECRH THEORY	11
2.1. Definition of geometry and dispersion function	11
2.2. Cut-offs and resonances for O- and X-waves	13
2.3. Density regimes in connection with ECRH	17
2.4. Wave absorption around harmonics of the electron cyclotron frequency	19
2.5. The O-X-B mode conversion scheme	25
3. RAY-TRACING	33
3.1. The ray equations	33
3.2. Dispersion functions used for ray-tracing	35
3.3. Definition of geometry and plasma equilibrium	38
3.4. O-X-B ray-tracing	40
4. PROFILE CALCULATIONS	43
4.1. Radial power density profiles	43
4.2. Radial current density profiles	44
4.3. Antenna modelling	45
5. NUMERICAL RESULTS	51
6. CONCLUSION	65
ACKNOWLEDGEMENTS	70
REFERENCES	71
APPENDICES	
A. Polarization of O- and X-waves	74
B. A general method for solving the ray equations in Cartesian coordinates	79

PREFACE

This report is written in order to meet part of the requirements for obtaining the Danish Ph.D. degree of lic.techn. My supervising professor is P.L. Ølgaard from the Department of Electrophysics at the Technical University of Denmark. As co-supervisors I have V.O. Jensen and P. Michelsen, both from Risø National Laboratory. The report contains results obtained in the period from January 1983 to April 1985 while I was attached to the ECRH Group in the Plasma Physics Division in the Department of Physics at Risø National Laboratory. My colleagues in the ECRH Group are P. Michelsen and J.P. Lynov, and as such they have a share in the results described.

1. INTRODUCTION

Throughout the entire period of controlled fusion research the central problems have been those of plasma heating and plasma confinement. In the beginning most of the effort was devoted to the confinement problem, and a major breakthrough came in the late 1960s. At that time the tokamak configuration showed highly improved confinement properties and the tokamak is now considered a possible candidate for a prospective fusion reactor. Unfortunately the plasma resistivity scales so unfavourably with the temperature in a tokamak that the initial ohmic heating alone will not raise the temperature to the required 10 keV. The necessity for additional heating has therefore been accepted, and various methods for such heating have been investigated more and more intensively throughout the past decade.

A variety of additional heating systems have been proposed. The most important schemes which are listed below can be divided into three main groups:

- High-energetic beams of neutral particles.

- Low-frequency or non-oscillatory fields.
  - Adiabatic compression
  - Transit Time Magnetic Pumping (TTMP) 10-200 kHz

- High-frequency electromagnetic waves.
  - Alfven wave heating 100 kHz - 10 MHz
  - Ion Cyclotron Resonance Heating (ICRH) 20-200 MHz
  - Lower Hybrid Resonance Heating (LHRH) 1- 10 GHz
  - Electron Cyclotron Resonance Heating (ECRH) 50-200 GHz

In order for the various heating schemes to meet the overall objective of ion heating without severe deteriorating the confinement properties, one must generally require that the power be delivered to the central part of the system and to the bulk of

the particle distributions. Most of the schemes meet these requirements only to a limited extent.

Neutral beam injection has proved effective on tokamaks of present day size and 3.1 MW of neutrals injected into the Princeton Large Torus (PLT) raised the ion temperature by approximately 6 keV to a record level of 7.1 keV (STODIECK et.al. (1981)). However, problems in future larger machines with denser plasmas are foreseen. Higher beam energies are necessary in order for the beams to penetrate into the central part of the system, but higher beam energies call for a considerable development of present systems such as direct energy recovery or alternatively development of advanced systems based on negative ions.

Experimental efforts on schemes using low-frequency and non-oscillatory fields are rather limited. Presumably these will play no significant role as major additional heating methods. Moreover, a large-scale application of TTMP seems to be impossible due to the occurrence of parametric instabilities in the relevant frequency range.

Since a magnetized plasma supports a variety of waves and contains a number of resonances, several schemes utilizing high-frequency electromagnetic waves have been proposed and investigated experimentally. The frequency range of interest covers almost seven orders of magnitude, indicating that the various schemes possess different advantages and disadvantages.

In the low frequency end of the scale, Alfven wave heating and ICRH are characterized by free-space wavelengths larger than or comparable to the plasma dimensions. For the schemes in this frequency range, units producing large amounts of power are already available, but the coupling of the power to the plasma is troublesome since large antennae placed close to the plasma boundary are required. Recent results indicate that Alfven wave heating leads to heating in the outer region of the plasma and thus to an enhanced impurity influx (DE CHAMBRIER et.al. (1984)). As the most highly developed RF-heating scheme, ICRH has experienced a great deal of success, and has been selected as the main

additional heating scheme on several tokamaks in operation and under preparation. The continued success depends mainly on the development of antennae capable of handling the many tens of MW needed to ignite a large plasma, and the ability to control the impurity level. A further development of antenna structures that couple the wave power effectively to the plasma and prevent edge heating is also very important for the scheme using waves at the lower hybrid frequency.

ECRH provides an extremely attractive alternative to the other schemes for two reasons. Both arise from the fact that the wavelengths in question are much shorter than the characteristic plasma dimensions. In the first place, the power may be coupled to the plasma with an efficiency of almost 100 per cent by simple waveguides. Secondly, the wave power may be delivered in a narrow region near the plasma centre, without affecting the plasma in the edge region.

Up to date ECRH has lagged behind other heating schemes since no powerful sources in the relevant frequency range existed. However, the development of the gyrotron oscillator has made ECRH possible. The performance of the gyrotrons has, however, not yet reached a level of significance for heating plasmas to ignition, and the future for ECRH depends to a large extent on the development of proper sources. Research has been initiated to produce microwave amplifiers with an output level around 1 MW at 100-150 GHz (FESTEAU-BARRIOZ et.al. (1984) and JORY (1984)).

A disadvantage of ECRH is that the ions are heated indirectly by transfer of energy from the electrons in electron-ion collisions, a relatively slow process. However, in anticipated large experiments where the electron energy confinement times are expected to exceed the times for the electron and ion temperatures to equilibrate this disadvantage will cease to be important. In any event, it should be noted that as the plasma temperature increases the electrons and ions decouple more and more and the energy transfer process noted above slows down.

Another more serious disadvantage of ECRH is the density limit connected to the scheme. This density limit is especially restrictive when the waves are launched conventionally (i.e. almost perpendicular to the magnetic field lines at the first harmonic of the electron cyclotron frequency) from the outside of the torus. In this case the waves are able to travel up to a certain critical density. The density limit is less restrictive when the waves are launched from the inside of the torus, in which case twice the critical density may be reached. However, an inside launch causes considerably more technical problems than an outside launch, which is therefore considered more attractive.

The density limit should indeed be taken seriously since prospective tokamaks like NET/INTOR are expected to operate in such a high-density regime that heating by waves launched conventionally from the outside becomes impossible (ENGELMANN (1984)).

Basically there are two distinct ways to get around the density limit problem: The first is to utilize waves at the second harmonic of the electron cyclotron frequency. One thereby pushes up the abovementioned density limit by a factor of two. Although it is likely that high-frequency oscillators of high power can be developed for heating by the fundamental frequency, even in large tokamak reactors with high fields, it seems as if a completely new technique is required for second harmonic heating.

The second is an entirely different method for heating an overdense plasma by waves at the fundamental of the electron cyclotron frequency from the outside of the torus. It has been suggested by PREINHAELTER and KOPECKY (1973). An essential part of this scheme is the conversion of the injected waves (O-waves) to another wavetype (X-waves) at the critical density layer. This mode conversion requires the O-waves to be injected near an optimal angle obliquely to the magnetic field lines. The X-waves propagate towards the upper hybrid resonance layer located near the outside of the torus, where they are converted into electron Bernstein waves (B-waves) which are completely absorbed close to the plasma centre. As a pleasent feature, the O-X-B mode con-

version scheme has no upper density limit connected to it, at least in principle.

In order to study the feasibility of the O-X-B mode conversion scheme in a tokamak plasma, an experiment to be performed in the Danish tokamak DANTE, has been planned. In connection with this experiment we have performed ray-tracing calculations in order to predict where in the plasma the ECRH power will be delivered. The remaining sections of the present work are organized as follows: Section 2 outlines the basic theory for ECRH. In this section the various possibilities for heating overdense plasmas are discussed, and the O-X-B mode conversion scheme is described in detail. Section 3 describes a ray-tracing program developed to study the O-X-B scheme, and Section 4 deals with the ECRH power deposition. Here the methods used to calculate the radial power density profiles and the associated wave-driven current density profiles are presented. In Section 5 some numerical results are given, and the paper ends with some concluding remarks in Section 6.

2. ECRH THEORY

2.1. Definition of geometry and dispersion relation

The fundamental physics of the various ECRH schemes is most easily studied in a slab geometry. As shown in Fig. 1 we will consider a slab with a static homogeneous magnetic field, $\underline{B}$, directed along the z-axis, and a density gradient directed along the x-axis.

Since the plasma is homogenous along the y- and z-directions, the y- and z-components of the wave vector, $\underline{k}$, for a plane electromagnetic wave of the form $\underline{A}\exp[i(k_x x+k_y y+k_z z - \omega t)]$ will be constant (Snell's law). However, since $\underline{k}$ is dependent on the plasma density, k_x will be a function of x. If the spatial densi-

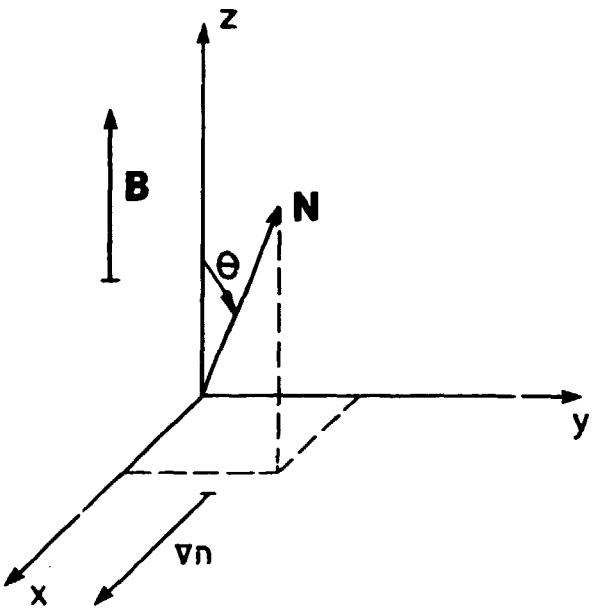

Fig. 1. Orientation of the magnetic field, B, the density gradient, ∇n, and the refractive index vector, N in the slab geometry.

ty variation is weak, i.e., if $k_x >> L_n^{-1}$, where $L_n = n/|\nabla n|$ is the density scale length, we may assume that k_x is locally determined by the dispersion relation for a homogenous plasma.

If the applied frequency, ω, is near the electron cyclotron frequency, ion dynamics may be ignored, and if the plasma can be considered as cold (the phase velocity of the waves exceeds the electron thermal velocity considerably), the waves will satisfy the Appleton-Hartree dispersion relation

$$N_x^2 + N_y^2 + N_z^2 = 1 - \frac{2X(1-X)}{2(1-X)-Y^2\sin^2\theta \pm \Gamma} \qquad (1)$$

where

$$\Gamma = \sqrt{Y^4\sin^4\theta + 4(1-X)^2Y^2\cos^2\theta}$$

$$X = \omega_{pe}^2/\omega^2$$

$$Y = \omega_{ce}/\omega$$

In the Appleton-Hartree dispersion relation (1), $\underline{N} = c\underline{k}/\omega$ is the refractive index vector and θ is the angle between the refractive index vector and the magnetic field. $\omega_{pe} = (ne^2/\varepsilon_o m_e)^{1/2}$ is the electron plasma frequency and $\omega_{ce} = eB/m_e$ is the electron cyclotron frequency. We will apply the usual terminology (see e.g. WEITZNER and BATCHELOR (1979)) and let the upper sign in Eq. (1) correspond to the ordinary (O) mode and the lower to the extraordinary (X) mode.

2.2. Cut-offs and resonances for O- and X-waves

The major characteristics of high-frequency wave propagation in a cold magnetoplasma is revealed by locating the cut-offs and resonances for the O- and X-waves. Without losing generality, we may assume that the waves propagate in the xz-plane, so N_y can be put equal to 0 in Eq. (1). In the slab geometry the waves are cut-off at densities where $N_x^2 = 0$ and a resonance appears where N_x^2 goes to infinity. The cut-off densities are found by letting $N_x = 0$ in Eq. (1) which may then be solved for X. The solutions are

$$X = \begin{cases} (1 \pm Y)(1-N_z^2) & \text{when } X < 1 \\ (1 \mp Y)(1-N_z^2) & \text{when } X > 1 \\ 1 & \text{always} \end{cases} \qquad (2)$$

In order to make a correct interpretation of the square root appearing in Eq. (1), the solution for X has branched out in a solution valid for $X < 1$ and one valid for $X > 1$. Furthermore, $X = 1$ turns out to be a solution for all possible N_z. This is however not apparent from the Appleton-Hartree dispersion relation, since $N_x^2 = 0$ and $X = 1$ simultaneously causes both the numerator and denominator to vanish. From an alternative description of high-frequency waves in a cold plasma, as the one in Appendix A, it is however easily demonstrated that $X = 1$ always yields a cut-off. It is seen that the two solutions for $X < 1$ and $X > 1$ are identical, except that the signs in front of Y are in-

terchanged, and Eqs. (2) therefore predict a maximum number of three solutions for X, for a given value of N_z.

The solution for X, valid for X > 1 does not represent a cut-off for the O-waves since any N_z makes X less than 1, which is in direct conflict with the assumption X > 1. On the other hand, the solution valid for X < 1 does represent a cut-off for the O-waves, but in order not to violate the inequality X < 1, we must require that $N_z^2 > Y/(1+Y)$. The solution for X, valid for X < 1 represents a cut-off for the X-waves for any N_z, since any N_z indeed makes X < 1. On the other hand, in order for the solution valid for X > 1 to represent a cut-off for the X-waves we must put a restriction on N_z. For the assumption X > 1 to hold, we must require that $N_z^2 < Y/(1+Y)$. A detailed analysis shows that the part of the X = 1 solution with N_z^2 lying in the range from 0 to Y/(1+Y) represents a cut-off for the O-mode and the remaining part a cut-off for the X-mode. The results are depicted in Fig. 2.

From the figure it is seen that the X-waves are everywhere cut-off at two places for a given value of N_z. The X-wave branch of the dispersion function the cut-off of which is represented by the solution in Eqs. (2) valid for X < 1 is called the fast X-wave branch, and the other branch is called the slow X-wave branch. In the special case of propagation parallel to the magnetic field lines the waves are circularly polarized (the expressions describing the wave polarization are derived in Appendix A). The fast X-wave is right-hand circularly polarized in the sense that the tip of the $\underline{E}$-field vector rotates counter clockwise at a fixed position in space when an observer looks toward the oncoming wave propagating in the same direction as the magnetic field lines.

From Fig. 2 it is seen that the fast right-hand circularly polarized X-wave is cut-off at X = 1-Y. This cut-off is therefore termed the right-hand cut-off, or simply the R cut-off. The O-waves and the slow X-waves are left-hand circularly polarized, and the slow X-wave cut-off at X = 1+Y is called the left-hand cut-off, or the L cut-off.

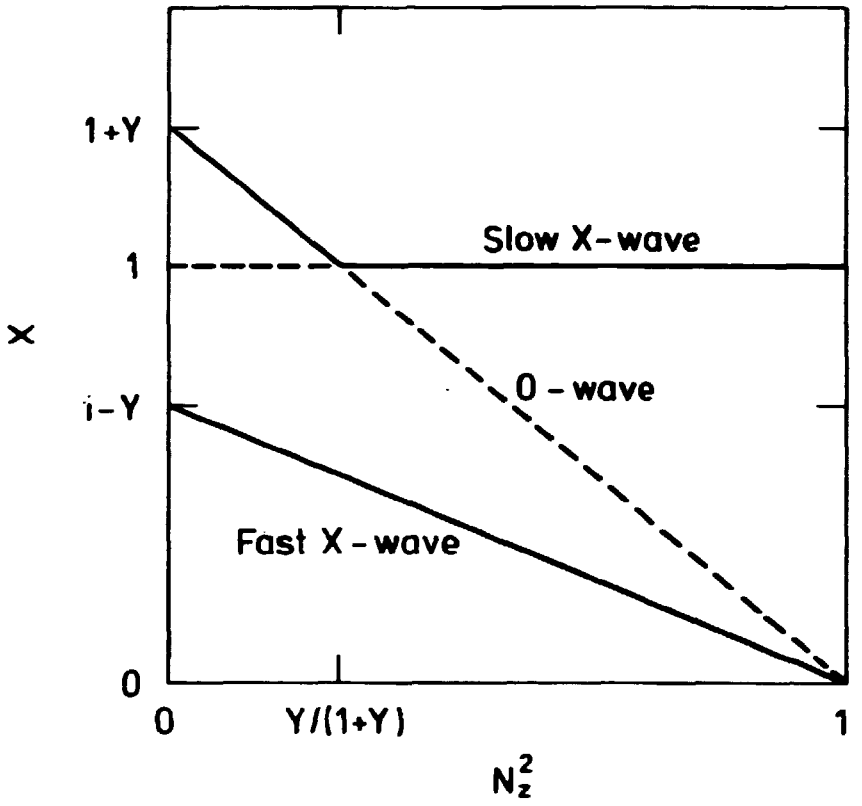

Fig. 2. Location of cut-offs for the O-mode and for the slow and the fast X-mode for varying N_z. The O- and X-mode cut-offs are shown by dashed and continuous curves, respectively.

When looking for resonances, we put the denominator of Eq. (1) equal to 0. By doing this, it turns out that only the X-waves experience a resonance. This appears at densities where $X = 1-Y^2$ and it is called the upper hybrid resonance.

Summarizing the results obtained above, we have found the following cut-off densities:

$$X = \begin{cases} \min[1,(1+Y)(1-N_z^2)] & \text{for the O-waves} \\ (1-Y)(1-N_z^2) & \text{for the fast X-waves} \\ \max[1,(1+Y)(1-N_z^2)] & \text{for the slow X-waves.} \end{cases} \quad (3)$$

Finally, the upper hybrid resonance for the slow X-waves is located at

$$X = 1-Y^2 \quad (4)$$

The results may also be viewed graphically in the CMA-diagram. The high-frequency part of the CMA-diagram is shown in Fig. 3.

The combinations of the parameters X and Y giving rise to the different cut-offs and resonances are represented by curves dividing the diagram into different regions. The CMA-diagram shown in Fig. 3 is drawn for propagation perpendicular to the magnetic field, i.e. N_z has been put equal to 0 in Eqs. (3) in order to obtain the curves. On the figure the R cut-off is labelled $\omega = \omega_R$, the L cut-off $\omega = \omega_L$, the plasma cut-off $\omega = \omega_{pe}$ and the upper hybrid resonance $\omega = \omega_{uh}$. Furthermore, the electron cyclotron resonance is labelled $\omega = \omega_{ce}$. It should, however, be noted that according to cold plasma theory, neither the O- nor the X-waves experience a resonance at the electron cyclotron resonance layer, and hence neither of the modes are damped according to cold plasma theory. Only when finite temperature effects are taken into account are the mechanisms accounting for the wave absorption included. Referring to the CMA-diagram in Fig. 3, the O-waves are cut-off at the line $X = 1$ and they cannot propagate at densities corresponding to the region to the right of $X = 1$. The X-waves can propagate for all combinations of X and Y, except for those corresponding to the shaded regions in Fig. 3.

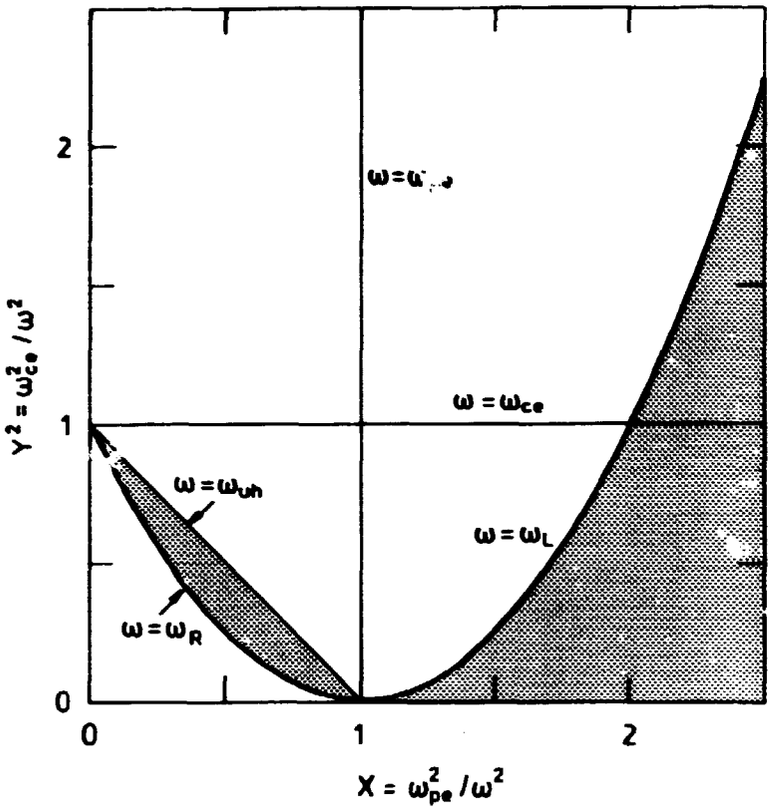

Fig. 3. The high-frequency part of the CMA-diagram for propagation perpendicular to the magnetic field lines. Shaded regions represent forbidden zones for the X-waves.

2.3. Density regimes in connection with ECRH

By assuming standard tokamak density and magnetic field profiles the location of the cut-off and resonance surfaces in a tokamak can be drawn. We consider a circular plasma equilibrium where the density varies parabolically as $X(r) = X(0)(1-r^2/a^2)$. Here $X(0)$ is the value of X at the centre of the plasma, a the minor radius of the torus and r a variable radius. The toroidal magnetic field strength varies as $Y_\phi(x) = Y_\phi(0)R/(R+x)$ where R is the major radius and R+x is the distance to the centre line of the torus. Finally the poloidal field is assumed to vary as $Y_\theta(r,x) = Y_\phi(x)r/R(1+2r^2/a^2)$. The locations of the cut-off and

resonance surfaces are determined by Eqs. (3) with $N_z = 0$ and $Y = (Y_\phi^2+Y_\theta^2)^{1/2}$. Figures 4a, 4b and 4c show poloidal cross sections of a low-density ($X(0) < 1$), a medium-density ($1 < X(0) < 2$) and a high-density ($X(0) > 2$) plasma, respectively. In all three cases the electron cyclotron resonance layer is located at the centre, i.e. $Y_\phi(0) = 1$. As in the CMA-diagram Fig. 3, the X-waves cannot propagate in the shaded regions.

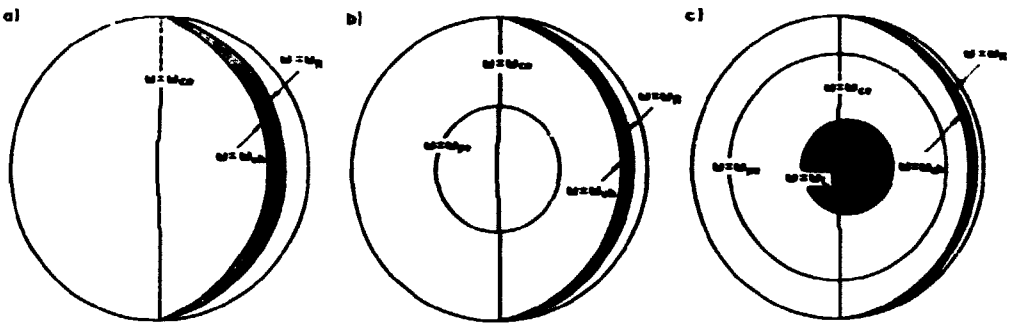

Fig. 4. Poloidal cross sections of a circular tokamak showing the location of the cut-off and resonance surfaces. Aspect ratio R/a = 3 and $Y_\phi(0) = 1$. The centre line of the torus is placed to the left of the figure. (a) Low-density plasma with X(0) = 0.75; (b) Medium-density plasma with X(0) = 1.20; (c) High-density plasma with X(0) = 2.20.

It is seen from Fig. 4a that X-waves launched from the low-field side of the torus cannot reach the cyclotron resonance since they are cut-off and hence reflected at the R cut-off layer near the outside of the torus. Central heating by waves launched from the outside is however possible, but only in the low-density case where O-waves may reach the cyclotron resonance. The maximum density, n_{max}, which can be heated by O-waves is given by

$$n_{max} = \varepsilon_o B^2/m_e \qquad (5)$$

In the medium-density case, the O-waves are reflected at the plasma cut-off and only X-waves injected from the inside may reach the central region. In this case a density corresponding to

two times n_{max} can be heated. In the high-density case shown in Fig. 4c neither the O- nor the X-waves are able to penetrate into the central region.

As mentioned in Section 1, the density limit may in fact turn out to put a severe constraint on the application of ECRH to future tokamak plasmas close to thermonuclear conditions. In the future, more dense plasmas will presumably inhibit the O-waves to penetrate into the central region. Though X-waves launched from the inside of the tokamak may reach twice the density of O-waves, an outside launch is considered a vital advantage over that of an inside one.

Central heating of overdense plasmas by waves launched from the outside is however still possible if the plasma is heated at the second harmonic or higher harmonics of the electron cyclotron frequency. From Eqs. (3) it may be realized that the maximum density, n^{ℓ}_{max}, which can be heated by waves at the ℓth harmonic ($\ell > 1$) of the cyclotron frequency is given by

$$n^{\ell}_{max} = \begin{cases} \ell^2 n_{max} & \text{for O-waves} \\ \ell(\ell-1) n_{max} & \text{for X-waves} \end{cases} \qquad (6)$$

Though in principle one can heat at arbitrarily high densities by choosing a suitable high frequency, in practice one is restricted to the first few harmonics. The choice of frequency is both limited by a relatively low single pass absorption at high harmonics of the cyclotron frequency and the lack of powerful sources opperating at very high frequencies. The question of the absorption of the waves will be treated in the next section.

2.4. Wave absorption around harmonics of the electron cyclotron frequency

The absorption and emission of waves around harmonics of the electron cyclotron frequency in fusion plasmas is a very large field in itself. A recent review covering theoretical as well as

experimental aspects has been given by BORNATICI et.al. (1983). Here we shall deal only with the main results, and in particular those relevant to overdense plasmas.

As mentioned in Section 2.2, cold plasma theory predicts no resonance and thus no absorption at $\omega = \omega_{ce}$. However, due to the finite temperature, the electrons gyrate around the magnetic field lines, and one will expect a resonant wave-particle interaction at $\omega = \omega_{ce}$. This is indeed the case, and, furthermore, due to the finite extension of the gyro orbits, resonant wave-particle interactions will also take place at harmonics $\omega = \ell\omega_{ce}$, $\ell = 1, 2, \ldots$ of the electron cyclotron frequency. Several mechanisms result in a broadening of the absorption lines. The most important line-broadening mechanism is due to the Doppler effect. Waves with wave number, k_z, (subscript z refers to the direction along the magnetic field lines) and angular frequency, ω, around the ℓth harmonic of the cyclotron frequency interact resonantly with electrons having a velocity, v_z, satisfying the Doppler condition

$$\omega = \ell\omega_{ce} + k_z v_z \tag{7}$$

When $k_z c/\omega < v_{te}/c$, where $v_{te}/c = (\kappa T_e/m_e c^2)^{1/2}$ is the ratio of the electron thermal speed to the speed of light in vacuum, the relativistic line-broadening mechanism becomes dominant. However, for almost all practical circumstances the relativistic line-broadening is important only for propagation that is almost perpendicular to the magnetic field.

A very important quantity in connection with ECRH is the fractional power absorbed by the plasma during a single pass of the waves through the resonance layer. This quantity is given by $1 - e^{-\tau}$, where τ is the optical thickness of the plasma. For the optical thickness, $\tau_\ell = \tau_\ell(\omega_{pe}, \omega_{ce}, T_e, \theta, R)$, of a tokamak plasma for waves at the ℓth harmonic of the cyclotron frequency we use the the expressions from BORNATICI (1982)

$$\tau_\ell = \begin{cases} 2\pi\tilde{R}\,\dfrac{\kappa T_e}{m_e c^2}\,N|\cos\theta|\,\dfrac{\omega_{ce}R}{c} & \text{for } \ell = 1 \\ \dfrac{\pi \ell^{2(\ell-1)}}{2^\ell(\ell-1)!}\,\dfrac{\omega_{pe}^2}{\omega_{ce}^2}(\sin^2\theta)^{(\ell-1)}\left(\dfrac{\kappa T_e}{m_e c^2}\right)^{(\ell-1)} & \\ \quad \times\,(1+\cos^2\theta)\mu_\ell\,\dfrac{\omega_{ce}R}{c} & \text{for } \ell > 2 \end{cases} \tag{8}$$

where

$$\tilde{R} = \left\{\frac{\left[(1-\omega_{pe}^2/\omega_{ce}^2)(1-\omega_{pe}^2/2\omega_{ce}^2-N^2\cos^2\theta)-N^2\sin^2\theta\right]^2}{(1-\omega_{pe}^2/\omega_{ce}^2-N^2\sin^2\theta)^2(a_1^2+b_1^2)^{1/2}}\right\}\frac{\omega_{ce}^2}{\omega_{pe}^2}\cos\theta$$

$$\mu_\ell = \frac{N^{2\ell-3}}{1+\cos^2\theta}\,\frac{(\ell-1)^2\left[1-(1+1/\ell)f_\ell\right]^2}{(a_\ell^2+b_\ell^2)^{1/2}}$$

$$a_\ell^2 = \left[1 + \frac{(1-\omega_{pe}^2/\ell^2\omega_{ce}^2)N^2\cos^2\theta}{(1-\omega_{pe}^2/\ell^2\omega_{ce}^2-N^2\sin^2\theta)^2}\ell^2\left(1-\frac{\ell^2-1}{\ell^2}f_\ell\right)^2\right]^2\sin^2\theta$$

$$b_\ell^2 = \left[1 + \frac{1-\omega_{pe}^2/\ell^2\omega_{ce}^2}{1-\omega_{pe}^2/\ell^2\omega_{ce}^2-N^2\cos^2\theta}\ell^2\left(1-\frac{\ell^2-1}{\ell^2}f_\ell\right)^2\right]^2\cos^2\theta$$

$$N^2 = 1 - \frac{\omega_{pe}^2}{\ell^2\omega_{ce}^2}f_\ell$$

$$f_\ell = \frac{2(\ell^2-\omega_{pe}^2/\omega_{ce}^2)}{2(\ell^2-\omega_{pe}^2/\omega_{ce}^2)-\sin^2\theta\pm\Gamma_\ell}$$

$$\Gamma_\ell = \left[\sin^4\theta+4(\ell^2-\omega_{pe}^2/\omega_{ce}^2)^2\cos^2\theta/\ell^2\right]^{1/2}$$

The expressions for τ_ℓ are valid in the Doppler regime, i.e. for

$k_z c/\omega > v_{te}/c$. The optical thickness for the O-mode is distinguished from that of the X-mode by the choice of sign in the expression for f_ℓ. As in Section 2.1 the upper sign must be used for the O-mode.

The expressions for τ_ℓ depend on too many parameters to allow a very detailed numerical investigation to be made. However, the favourable scaling of τ_ℓ with increasing temperature and major radius is quite obvious and we shall instead consider a specific example, which to a large extent displays the general behaviour of τ_ℓ. We consider a tokamak of PLT size with B = 2.14 T and R = 1.32 m. Figures 5a and 5b show the variation of the fractional power absorbed with injection angle, θ, and electron temperature, T_e, for O-waves (Fig. 5a) and X-waves (Fig. 5b) at the fundamental of the electron cyclotron frequency. In both cases the density is 0.75 times the maximum density which can be heated, i.e. $n = 0.75 n_{max}$. It should be noted that θ in Eqs. (8) refers to the angle between the wave vector and the magnetic field at the cyclotron layer, whereas θ in the figures refers to the same angle at the plasma boundary. In this connection, the value of N_z is assumed to remain constant for the injected waves. Though this is not entirely correct, it is a good approximation for waves injected in the mid-plane of the torus over a wide range of angles that are nearly perpendicular to the magnetic field.

From Fig. 5a it is seen that the O-waves are almost completely absorbed over a large range of injection angles when the temperature exceeds a few keV. In general, O-waves at the fundamental frequency suffer almost complete damping in large hot tokamak plasmas, provided that the density lies below the cut-off value for the O-mode. Recent experiments on T-10 (ALIKAEV and PARAIL (1984)), PDX (HSUAN et.al (1984)) and Doublet III (PRATER et.al. (1984)) have proved that this method is effective for localized and central heating.

In small devices the O-waves are only slightly damped, and in a tokamak like DANTE with B = 0.625 T, R = 0.50 m, T_e = 0.2 keV and $n = 2.9 \cdot 10^{19}$ m^{-3} the single-pass absorption will be as low as 4 per cent.

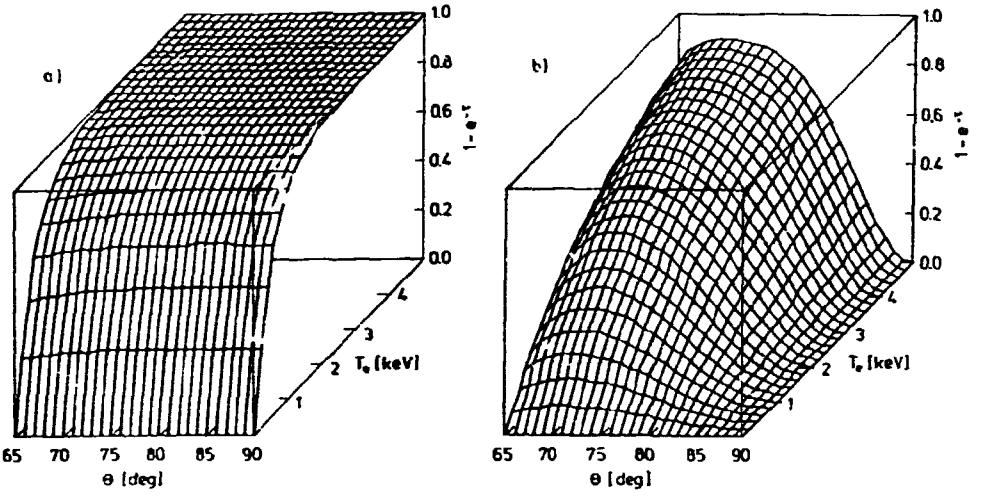

Fig. 5. Fractional single-pass absorption for O- and X-waves at the fundamental of the electron cyclotron frequency in a tokamak plasma. θ is the injection angle and T_e the electron temperature at the resonance layer. R = 1.32 m, B = 2.14 T. (a) O-wave absorption. $n = 0.75 n^1_{max} = 3.34 \cdot 10^{19}$ m^{-3}; (b) X-wave absorption. $n = 0.75 n^1_{max} = 6.68 \cdot 10^{19}$ m^{-3}.

From Fig. 5b it is seen that the optimal injection angle for X-waves at the fundamental frequency is oblique to the magnetic field. The single-pass absorption is generally poorer than for the O-waves. However, in large hot plasmas the X-waves will be almost completely absorbed. In the Doublet III experiment heating by inside launched X-waves at densities above the one corresponding to the O-mode cut-off has been observed.

In Figs. 6a and 6b the fractional single-pass absorption for O- and X-waves at the second harmonic of the cyclotron frequency is shown. As before the densities are 0.75 times the maximum densities which can be heated.

It is seen from Fig. 6a that the absorption of O-waves at the second harmonic is rather poor even at high temperatures. In small and moderate size tokamaks this mode will be of no

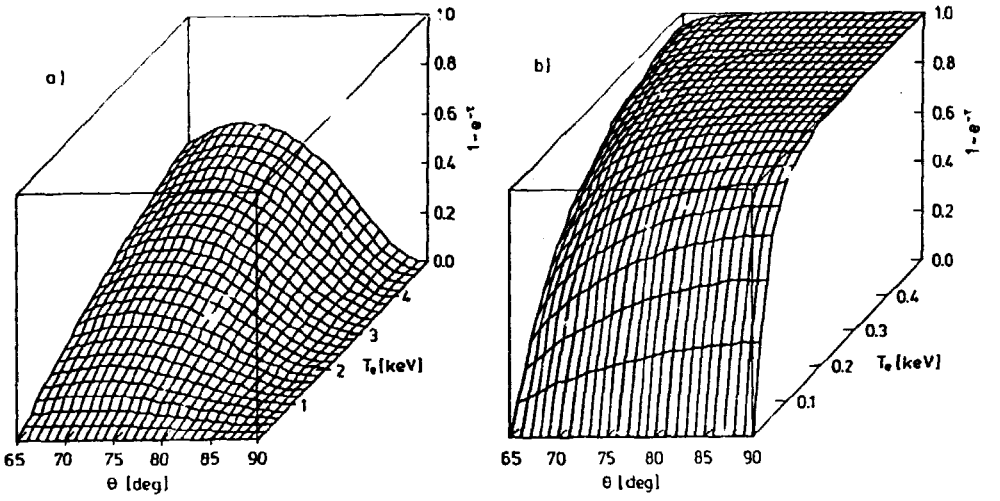

Fig. 6. Fractional single-pass absorption of O- and X-waves at the second harmonic of the cyclotron frequency in a tokamak plasma. R = 1.32 m, B = 2.14 T. (a) O-wave absorption. $n = 0.75n^2_{max} = 1.34 \cdot 10^{20}$ m^{-3}; (b) X-wave absorption. $n = 0.75n^2_{max} = 6.68 \cdot 10^{19}$ m^{-3}.

interest. However, in very large machines like JET and NET/INTOR, the second harmonic O-mode will suffer almost complete damping, and this scheme could be of importance in connection with large devices with densities ranging from two to four times the critical value. Below these densities the second harmonic X-mode could be used. This is seen from Fig. 6b which shows that this mode is strongly absorbed. This mode can even be used on small tokamaks with low temperature (see e.g. RIVIERE et.al. (1984)). On DANTE, the single-pass absorption will be approximately 40 per cent at $n = 5.7 \cdot 10^{19}$ m^{-3}.

The single-pass absorption at harmonics higher than the second is generally lower than at the first and the second harmonic, except at the third harmonic X-mode which is comparable to the second harmonic O-mode. In any case, efficient heating at harmonics of the cyclotron frequency in large tokamak reactors will probably be limited by the capacity of the microwave sources rather than by the absorptivity of the plasma.

2.5. The O-X-B mode conversion scheme

A quite different scheme which can be applied to overdense plasmas and which uses O-waves at the fundamental of the electron cyclotron frequency has been suggested by PREINHAELTER and KOPECKY (1973). A very important part of this scheme is the conversion from O- to X-waves at the plasma cut-off layer.

From the Appleton-Hartree dispersion relation (1) it is seen that the dispersion branches belonging to the O- and the X-waves coalesce when $\Gamma = 0$. By inspection of the expression for Γ this is seen to occur when $X = 1$ and $\theta = 0$ simultaneously. Equivalently it could be stated that coalescense occurs when both N_x and N_y equal 0 at the critical density where $X = 1$. More information about the coalescense is obtained from Eqs. (3). The first and last equations in (3) state that both the O- and the slow X-wave are cut-off at $X = 1$, however only when N_z^2 takes the optimal value

$$N_{z,opt}^2 = Y/(1+Y) \tag{9}$$

The variation of N_x^2 from Eq. (1) with X for fixed Y and different values of N_z is shown in Fig. 7.

It is seen that on entering the plasma from vacuum, the fast X-wave reaches a partial cut-off before the O-wave. Near the critical density, where the O-mode and the slow X-mode dispersion branches are connected, there generally is a region of evanescense. If $N_z < N_{z,opt}$ and $N_y = 0$ the X-waves are evanescent in a region above the critical density, and if $N_z > N_{z,opt}$ and $N_y = 0$ the O-waves are evanescent in a region below the critical density. Only if $N_z = N_{z,opt}$ and $N_y = 0$ will the region of evanescense disappear and N_x remain real across the $X = 1$ boundary.

It has been shown by PREINHAELTER and KOPECKY (1973) that an incident O-wave satisfying the conditions $N_z = N_{z,opt}$ and $N_y = 0$ at $X = 1$ is totally converted into an X-wave which propagates towards higher densities. If N_z deviates from $N_{z,opt}$ or if N_z is different from 0, the conversion will not be total, but the incident O-wave will be split up into a transmitted X-wave and re-

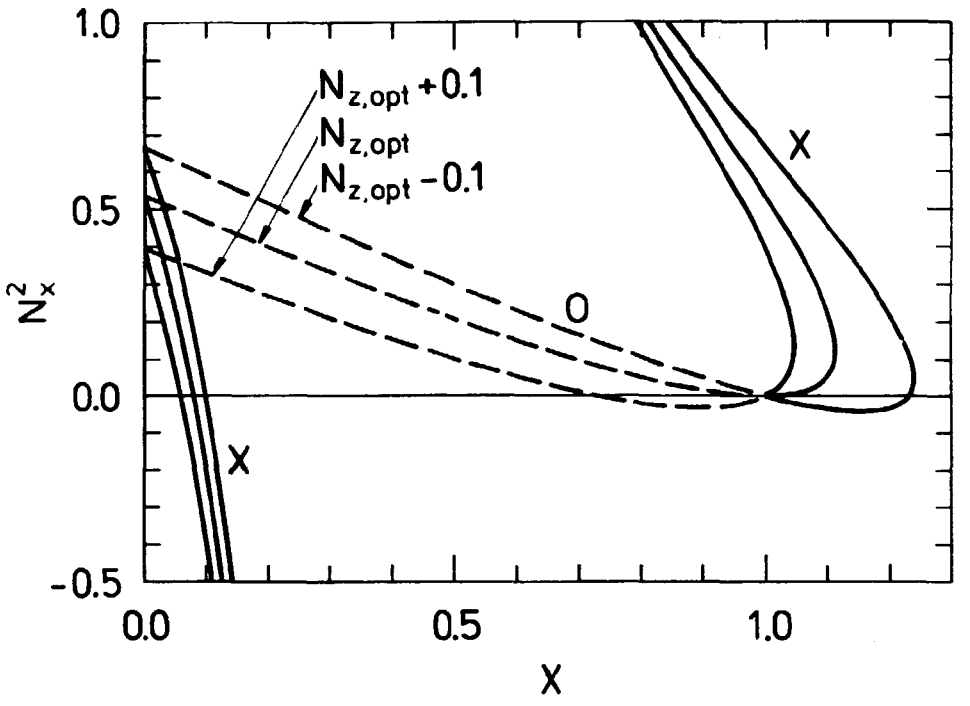

Fig. 7. N_x^2 versus X for different values of N_z. The O-waves are represented by dashed lines and the X-waves by continuous lines. Y = 0.85, N_y = 0 and $N_{z,opt}$ = 0.678.

flected O-wave near X = 1. In this case the power transmission coefficient for the conversion from O- to X-waves is (PREINHAELTER (1975))

$$T = \exp\{-\pi k_o L_n \sqrt{Y/2}[(N_{z,opt}^2 - N_z^2)^2 (1+Y)^2/2Y + N_y^2]\} \qquad (10)$$

where L_n and Y must be evaluated at the conversion point.

Since N_z is conserved in the plasma slab, the injection angle, i.e. the angle between the magnetic field vector and the wave vector at the plasma boundary, can be determined. This angle is called the optimal injection angle and is given by

$$\theta_{opt} = \text{Arccos}(N_{z,opt}) \qquad (11)$$

After conversion it is seen from Fig. 7 that the X-waves propagate toward the high-density region until they reverse and propagate toward the upper hybrid resonance layer, where $X = 1-Y^2$. According to cold plasma theory, the value of N_x^2 goes to infinity when the wave approaches the resonance layer, and consequently the phase velocity of the wave goes to zero. When the phase velocity of the wave approaches the electron thermal velocity finite temperature effects have to be taken into account, and as a result the slow X-wave is converted into a backward-propagating Bernstein (B) wave (PURI et.al. (1973)). The B-waves generated at the upper hybrid resonance layer propagate towards higher densities and they are strongly absorbed around the cyclotron harmonics if the angle between $\underline{N}$ and $\underline{B}$ is not exactly 90^o. In all the cases studied, the slow X- and the B-waves belong to the same branch of the hot dispersion relation, and the transfer of energy from the X- to the B-wave is 100 per cent. If, however, collisional, parametric decay or second harmonic generation processes, which are not included in the simple theory, are important, the energy transfer around the upper hybrid frequency will be modified.

Once the value of N_x is determined from the Appleton-Hartree dispersion equation (1), the polarization of the electric field can be calculated. A derivation of the $\underline{E}$-field polarization is presented in Appendix A, and in Fig. 8 we show the polarization of the O- and X-waves in the case of an O-wave incident at an optimal angle, corresponding to the curve labelled $N_{z,opt}$ in Fig. 7. The components of the electric field vector are everywhere normalized such that $|\underline{E}| = 1$.

It is seen that the O-wave polarization is more or less constant up to $X = 1$. At the $X = 1$ boundary the O- and X-wave part of the electric field polarization matches perfectly and there is a smooth transition of the $\underline{E}$-field at the O-X conversion point. The X-wave polarization changes much more radically, and as one approaches the upper hybrid resonance layer from the high-density side, the x-component of the electric field vector tends to be the dominant one. Since the x-component of the refractive index vector also becomes much larger than the y- and z-com-

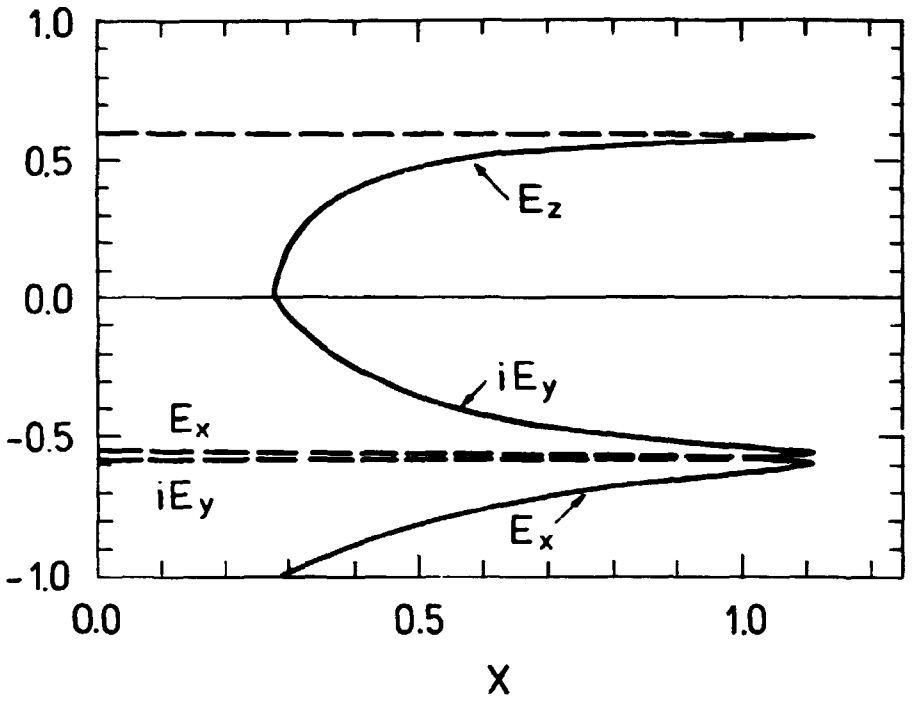

Fig. 8. Normalized components of the electric field vector for the O- and X-waves in the case of an O-wave incident at optimal angle. The O- and X-wave polarization are represented by dashed and continous curves, respectively. Y = 0.85.

ponents at the upper hybrid layer, the electrostatic nature of the slow X-wave close to the upper hybrid layer becomes more and more pronounced.

Besides possible losses at the plasma cut-off layer in connection with the O-X mode conversion process and the possible losses at the upper hybrid resonance layer, there may be losses at the point of injection due to polarization mismatches. An electromagnectic wave incident upon a magnetized plasma will generally excite both the O- and X-waves. Only in the case of perpendicular propagation are the O- and X-waves linearly polarized at the plasma boundary. If the injection angle differs from 90°, the incident waves must be elliptically polarized to excite either O- or X-waves. If, however, the polarization is linear at propagation angles different from 90°, the largest fraction of power is contained in the O-mode if the incident wave is polarized with the

electric field vector lying in the plane spanned by the wave vector and the magnetic field. In Appendix A a derivation is given of the wave polarization required to excite either of two modes for an arbitrary injection angle. An expression for the relative O-mode power content, η_O, in a linearly polarized wave is also given in Appendix A, and in Fig. 9 the variation with η_O for two different values of Y is shown.

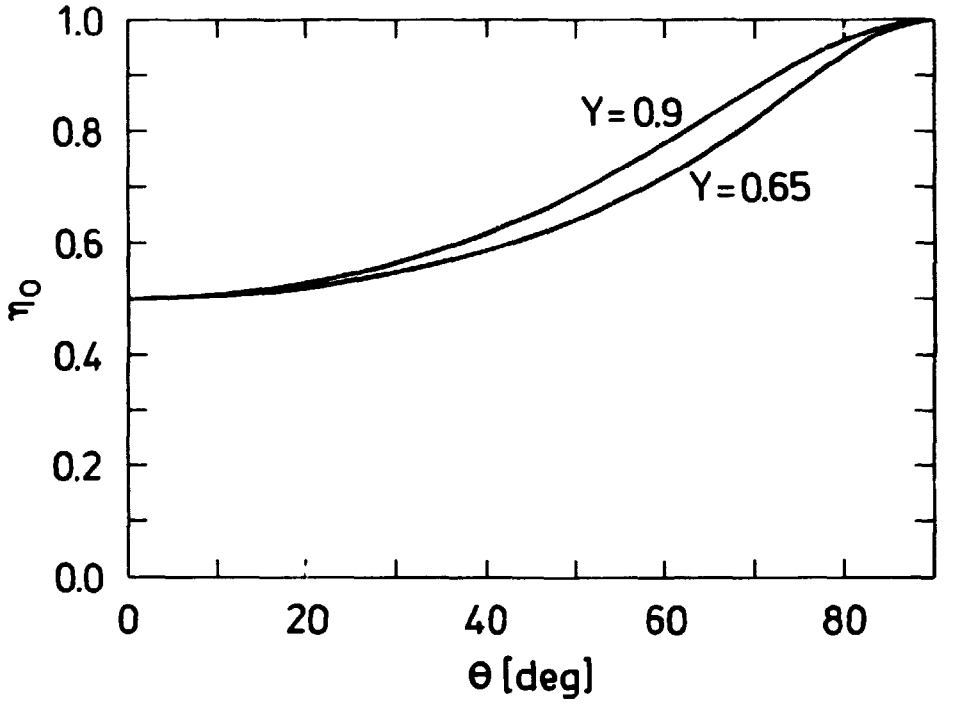

Fig. 9. O-mode power content, η_O, relative to the total power content in a linearly polarized wave incident upon a magnetized plasma. The incident wave is polarized with the electric field vector lying in the NB-plane. θ is the angle between N and B.

Up to this point we have investigated the O-X-B mode conversion scheme in a slab geometry. The effects on the optimal injection angle arising from a toroidal geometry are, however, easily taken into account if certain assumptions are made. We consider a toroidal plasma equilibrium identical to the one used to discuss the various density regimes shown in Fig. 4, except that we neglect the weak poloidal field. We assume that the waves are in-

jected in the mid-plane of the torus at an angle θ to the magnetic field. Since the poloidal field has been neglected, the waves are not refracted in poloidal direction. As shown by DE LUCA and MAROLI (1978), the product of the ϕ-component of the refractive index vector and the distance to the centre line of the torus

$$N_\phi(R+x) = \text{constant} \tag{12}$$

for waves propagating in a toroidal plasma equilibrium that is independent of the toroidal angle ϕ. Equation (12) is used to obtain a relation between the injection angle θ and the value of N_ϕ inside the plasma. In this relation, we may however replace N_ϕ by N_z since the poloidal field has been neglected, and the relationship between N_z and θ becomes

$$N_z(x) = \left[(R+a)/(R+x)\right]\cos\theta \tag{13}$$

An expression for the optimal angle in a toroidal plasma may now be obtained by combining Eqs. (9) and (13). We find that

$$\theta_{opt} = \text{Arccos}\left(\frac{R+x_c}{R+a}\sqrt{\frac{Y_\phi(x_c)}{1+Y_\phi(x_c)}}\right) \tag{14}$$

where $x_c = a\left[1-1/X(0)\right]^{1/2}$ is the position of the plasma cut-off layer. An example of the variation of the optimal angle for varying central density is shown in Fig. 10 for three different values of $Y_\phi(0)$. The curves in the figure are plotted for a fixed value of the aspect ratio, R/a.

It is seen that the optimal injection angle to the magnetic field lines typically lies around 50^o, even for relatively large variations of the density and position of the electron cyclotron resonance layer.

Clearly, it is very important for the O-X-B conversion scheme that a large fraction of the incident O-waves is converted into

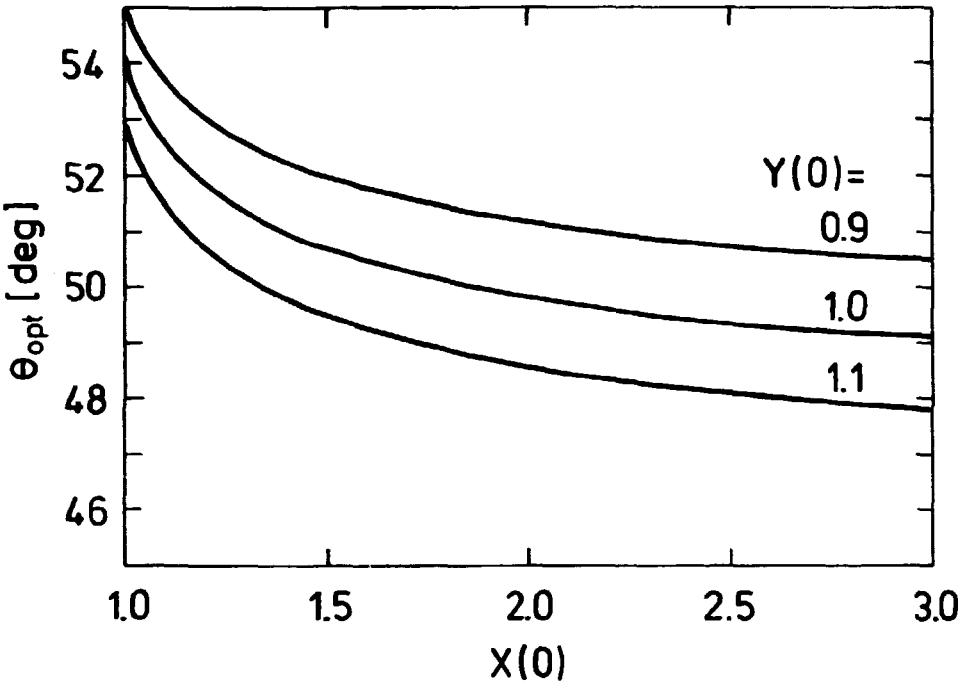

Fig. 10. Variation of the optimal angle, θ_{opt}, for varying central density in a toroidal plasma equilibrium. R/a = 4.55.

X-waves at the plasma cut-off layer. To ensure an overall high O-X mode conversion efficiency the O-waves must be injected in a narrow cone around the optimal angle, and from Eq. (10) an estimate of how narrow this cone should be can be obtained. Figure 11 show how the O-X transmission coefficient depends on the injection angle, θ, in two different situations, a low-frequency case (f = 17.5 GHz) and a high-frequency one (f = 60 GHz). These figures are relevant for respectively the DANTE and PLT tokamak. The value of N_z in Eq. (10) is related to the injection angle as given by Eq. (13).

From the figure it may be seen that the full width at 50 per cent O-X transmission for the curve corresponding to f = 17.5 GHz is approximately 14°, whereas the other curve is considerably narrower (approximately 2°). These numbers indicate that the requirement that the collimation of the antenna beams be used for the O-X-B scheme is most severe at high frequencies.

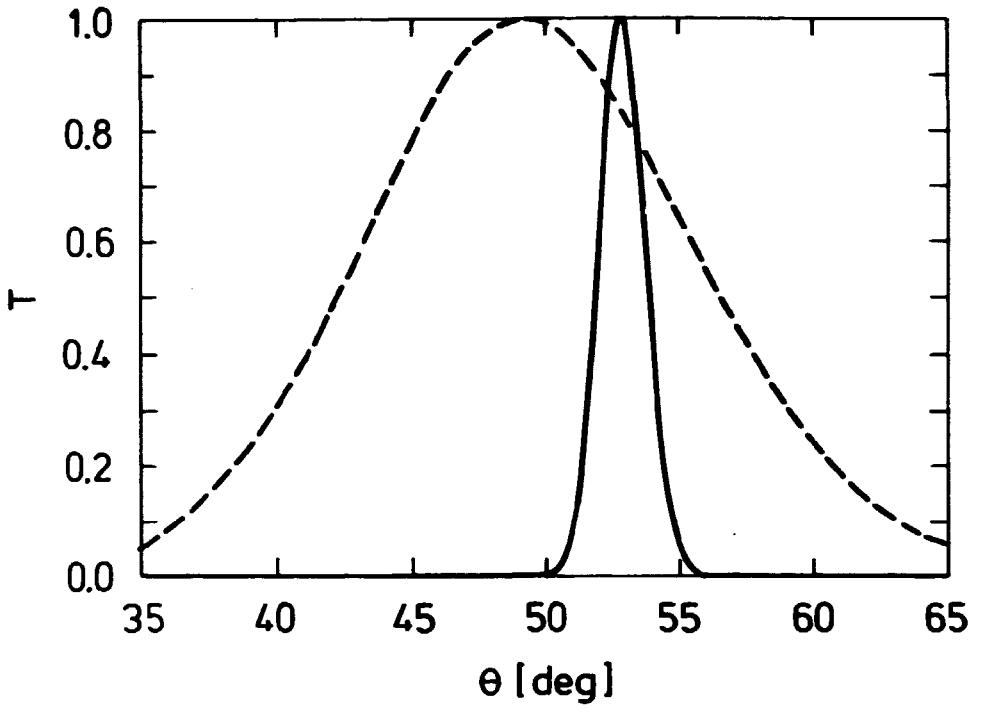

Fig. 11. O-X power transmission coefficient, T, as function of the injection angle, θ, for waves injected in the mid-plane of a torus. Y(0) = 1.00 for both curves. R = 0.50 m, a = 0.11 m, X(0) = 2.63 and k_o = 367 m^{-1} for the dashed curve. R = 1.32 m, a = 0.40 m, X(0) = 1.34 and k_o = 1257 m^{-1} for the continous curve.

It should, however, be noted that the widths of the transmission curves also depend on the density scale length and the magnetic field intensity at the plasma cut-off layer.

Finally, it should be mentioned that the conversion at the upper hybrid layer from X- to B-waves is also important for the ECRH scheme which uses X-waves at the fundamental frequency from the inside of the torus. This X-B mode conversion scheme has been studied on the Wendelstein VII-A stellarator (WILHELM et.al. (1984)). Unfortunately, no increase in the central electron temperature has been measured. Whether or not this negative result is due to special stellarator effects or is an unavoidable fundamental problem of the X-B mode conversion process is not apparent.

3. RAY-TRACING

For most ECRH experiments the wavelengths used are much shorter than characteristic plasma scale lengths. This allows the problem of determining the wave propagation to be treated by ray-tracing techniques. The validity of ray-tracing is directly related to the WKB conditions of weak spatial variation of the medium over distances of a wavelength and slow time variation of the medium during a single wave period. A more detailed description of the conditions which must be fulfilled in order to apply ray-tracing techniques to wave propagation problems in plasmas has been given by BORNATICI and ENGELMANN (1983).

In order to investigate the O-X-B mode conversion scheme in more complex geometries than the simple slab, we have developed a ray-tracing program, CONRAY. Ray-tracing studies of the O-X-B conversion scheme have been performed previously by MAEKAWA et.al. (1978) and (1980), but without introducing a full toroidal description of the plasma, as the one to be presented in this section.

3.1. The ray equations

We assume that the wave propagation is everywhere governed by the disperson relation for a homogenous plasma. A general form of the dispersion function is (STIX (1962))

$$D(\underline{r},\underline{k},\omega) = \det\{\underline{\underline{K}}(\underline{r},\underline{k},\omega) - (c^2/\omega^2)[(\underline{k}\cdot\underline{k})\underline{\underline{I}} - \underline{k}\underline{k}]\} \qquad (15)$$

where $\underline{\underline{K}}$ is the dielectric tensor and $\underline{\underline{I}}$ is the unit tensor.

A ray trajectory, $\underline{r}(t)$, i.e. a path of energy flow, is determined by solving the ray equations consisting of the six coupled, first-order, ordinary, differential equations

$$\frac{d\underline{r}}{dt} = -\frac{\partial D}{\partial \underline{k}} \Big/ \frac{\partial D}{\partial \omega}$$

$$\frac{d\underline{k}}{dt} = \frac{\partial D}{\partial \underline{r}} \Big/ \frac{\partial D}{\partial \omega} \qquad (16)$$

with initial values $\underline{r}(0)$ and $\underline{k}(0)$ satisfying the dispersion relation, i.e. $\underline{r}(0)$ and $\underline{k}(0)$ satisfying the condition

$$D(\underline{r}(0),\underline{k}(0),\omega) = 0. \qquad (17)$$

The parameter, t, along the ray trajectories correspond to the actual time.

In general $\underline{\underline{K}}$ consists of Hermitian and anti-Hermitian parts, the latter accounting for the absorption of the waves and giving rise to a complex D. If D is complex, the ray equations show that $\underline{r}$ and $\underline{k}$ become complex, corresponding to propagation in complex space. The interpretation of this phenomenon is not trivial, and has been studied by several authors (see e.g. BUDDEN and TERRY (1971) and CONNOR (1980)). However, if the elements in the anti-Hermitian part of the dielectric tensor are small compared to the elements in the Hermitian part, corresponding to weak damping, the rays are not seriously affected by the anti-Hermitian part of $\underline{\underline{K}}$. The rays may then be traced on the basis of a dispersion function where the anti-Hermitian part of the dielectric tensor has been neglected.

The ray equations (16) are expressed in Cartesian coordinates. It is, however, possible to formulate the ray equations in curvilinear coordinates (BRANDSTATTER (1963)) and DE LUCA and MAROLI (1978) used this formalism to perform ray-tracing calculations in toroidal coordinates.

Since plasma equilibria often are described in curvilinear coordinates, it seems reasonable to transform the ray equations to the curvilinear coordinates in question. By doing this, the description of the plasma equilibrium takes its simplest form, but one pays the price of a simple equilibrium by a set of more complicated ray equations, which moreover are restricted to the special geometry under consideration. Alternatively, one could solve the ray equations (16) in Cartesian coordinates as they stand. In this case one pays the price of simple looking ray equations by a more complex description of the plasma equilibrium, but since the geometry has not been fixed beforehand, one is left with a considerably more flexible system of equations. The latter method is the one used by CONRAY.

Though the ray equations are solved in Cartesian coordinates, the right-hand sides of the equations are first found in a local Cartesian coordinate system defined by the directions of $\underline{B}$ and $\underline{k}$, and they are subsequently transformed back to the global coordinate system. This procedure is similar to the one used by BATCHELOR et.al. (1980) and a detailed description of the equations involved in this method is given in Appendix B.

3.2. Dispersion functions used for ray-tracing

The ray-tracing calculations presented are based on two different dispersion functions. One for a cold plasma and one for a hot, non-relativistic, non-drifting plasma with isotropic temperature and Maxwellian particle distributions. In both cases ion dynamics are ignored. Both dispersion functions are related to a coordinate system where the magnetic field is directed along $\hat{z}$ and the wave vector lies in the right half-plane of the xz-plane.

The cold dispersion function used in CONRAY is similar to the Appleton-Hartree dispersion relation (1), but is written in the form

$$D = 1 - N_x^2 - N_z^2 - \frac{2X(1-X)}{2(1-X)-Y^2\sin^2\theta \pm \Gamma} \tag{18}$$

where

$$\Gamma = \sqrt{Y^4\sin^4\theta + 4(1-X)^2Y^2\cos^2\theta}$$

$$\sin^2\theta = N_x^2/(N_x^2+N_z^2)$$

$$\cos^2\theta = N_z^2/(N_x^2+N_z^2)$$

For the hot dispersion function the dielectric tensor is defined by

$$\underline{\underline{K}} = \begin{pmatrix} K_{xx} & K_{xy} & K_{xz} \\ -K_{xy} & K_{yy} & K_{yz} \\ K_{xz} & -K_{yz} & K_{zz} \end{pmatrix} \tag{19}$$

and by combining Eqs. (15) and (19) one obtains

$$D = \begin{vmatrix} K_{xx}-N_z^2 & K_{xy} & K_{xz}+N_xN_z \\ -K_{xy} & K_{yy}-N_x^2-N_z^2 & K_{yz} \\ K_{xz}+N_xN_z & -K_{yz} & K_{zz}-N_x^2 \end{vmatrix} \tag{20}$$

By introducing the new quantities $C_{xy} = -iK_{xy}$, $C_{xz} = K_{xz}/N_x$ and $C_{yz} = -iK_{yz}/N_x$ in Eq. (20), the dispersion function may be written in the form

$$D = AN_x^4 + BN_x^2 + C \tag{21}$$

where

$$A = 2C_{xz}N_z + K_{xx} + C_{xz}^2$$

$$B = 2C_{xz}N_z^3 + (K_{xx} + K_{zz} + C_{yz}^2 + C_{xz}^2)N_z^2$$

$$- 2(C_{xy}C_{yz} + K_{yy}C_{xz})N_z - K_{xx}(K_{yy} + K_{zz}) \tag{22}$$

$$+ C_{xy}^2 - K_{xx}C_{yz}^2 - 2C_{xz}C_{yz}C_{xy} - C_{xz}^2K_{yy}$$

$$C = K_{zz}[N_z^4 - (K_{xx}+K_{yy})N_z^2 + K_{xx}K_{yy} - C_{xy}^2]$$

The quantities appearing in the expressions for A, B an C are given by

$$K_{xx} = 1 + B_{xx} \sum_{n=0}^{\infty}{}' n^2 I_n(\lambda)[Z(\zeta_n) + Z(\zeta_{-n})]$$

$$C_{xy} = -B_{xy} \sum_{n=0}^{\infty}{}' n[I_n(\lambda) - I_n'(\lambda)][Z(\zeta_n) - Z(\zeta_{-n})]$$

$$C_{xz} = -B_{xz} \sum_{n=0}^{\infty}{}' nI_n(\lambda)[-Z'(\zeta_n) + Z'(\zeta_{-n})]/2$$

$$K_{yy} = 1 + B_{yy} \sum_{n=0}^{\infty}{}' [n^2 I_n(\lambda) + 2\lambda^2[I_n(\lambda) - I_n'(\lambda)]] \qquad (23)$$

$$\cdot [Z(\zeta_n) + Z(\zeta_{-n})]$$

$$C_{yz} = -B_{yz} \sum_{n=0}^{\infty}{}' [I_n(\lambda) - I_n'(\lambda)][\zeta_n Z(\zeta_n) + \zeta_{-n} Z(\zeta_{-n})]$$

$$K_{zz} = 1 - B_{zz} \sum_{n=0}^{\infty}{}' I_n(\lambda)[\zeta_n Z'(\zeta_n) + \zeta_{-n} Z'(\zeta_{-n})]$$

where

$$B_{xx} = X\zeta_o e^{-\lambda}/\lambda$$

$$B_{xy} = X\zeta_o e^{-\lambda}$$

$$B_{xz} = Xe^{-\lambda}/YN_z\lambda$$

$$B_{yy} = B_{xx} \qquad (24)$$

$$B_{yz} = Xe^{-\lambda}/YN_z$$

$$B_{zz} = B_{xy}$$

In connection with the summation symbols in the expressions above, the prime denotes that only half of the first term in the series contributes to the sums. In the numerical calculations the infinite series are truncated after a finite number of terms. This number is adjusted during the calculations so that the ratio of the last term to the sum of all the terms is less than 10^{-11}. An upper limit of terms is, however, set to 20.

I_n is the modified Bessel function of the first kind and order n (ABRAMOWITZ and STEGUN (1972)), and Z is the plasma dispersion function (FRIED and CONTE (1961)). The arguments λ and ζ_n are defined as

$$\lambda = N_x^2\gamma^2/Y^2 \qquad (25)$$

and

$$\zeta_n = (1+nY)/\sqrt{2}|N_z|\gamma \qquad (26)$$

where $\gamma = v_{te}/c = (\kappa T_e/m_e c^2)^{1/2}$ is the ratio of the electron thermal speed to the speed of light.

3.3. Definition of geometry and plasma equilibrium

The ray-tracing results in the present work are based on the following toroidal plasma equilibrium describing the electron density, electron temperature and magnetic field configuration.

$$n(r) = n(0)[1 - (r/a)^2]$$

$$T_e(r) = T_e(0)\left[1 - (r/a)^2\right]^2$$

$$B_\phi(r,\theta) = B_\phi(0)R/(R+r\cos\theta) \qquad (27)$$

$$B_\theta(r,\theta) = rB_\phi(r,\theta)/Rq(r)$$

$$q(r) = q(0) + \left[q(a)-q(0)\right](r/a)^2$$

The toroidal coordinate system is defined in Fig. 12.

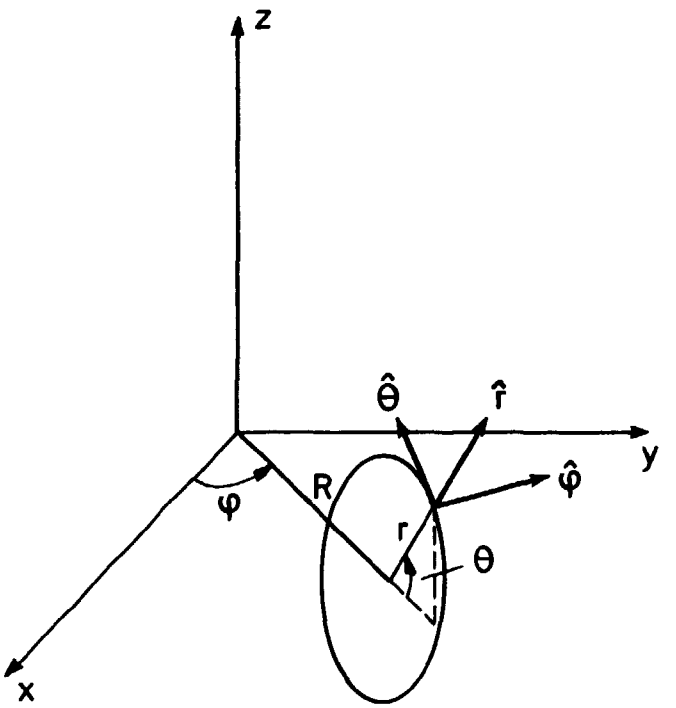

Fig. 12. Definition of the toroidal coordinate system used to specify the plasma equilibrium.

The coordinates x, y and z in the global coordinate system are related to the toroidal coordinates r, θ and θ as follows

$$\begin{pmatrix} x \\ y \\ z \end{pmatrix} = \begin{pmatrix} (R+r\sin\theta)\cos\phi \\ (R+r\cos\theta)\sin\phi \\ r\sin\theta \end{pmatrix} \qquad (28)$$

and the unit base vectors in the two coordinate systems are related as

$$\begin{pmatrix} \hat{x} \\ \hat{y} \\ \hat{z} \end{pmatrix} = \underline{\underline{J}}_1 \begin{pmatrix} \hat{r} \\ \theta \\ \hat{\phi} \end{pmatrix} \tag{29}$$

where

$$\underline{\underline{J}}_1 = \begin{pmatrix} \cos\theta\cos\phi & -\sin\theta\cos\phi & -\sin\phi \\ \cos\theta\sin\phi & -\sin\theta\sin\phi & \cos\phi \\ \sin\theta & \cos\theta & 0 \end{pmatrix} \tag{30}$$

The magnetic field in the global coordinate system is then given by

$$\begin{pmatrix} B_x \\ B_y \\ B_z \end{pmatrix} = \underline{\underline{J}}_1 \begin{pmatrix} B_r \\ B_\theta \\ B_\phi \end{pmatrix} \tag{31}$$

with $B_r = 0$.

The gradients ∇n, ∇T_e and $\nabla \underline{B}$ which are also required in performing the ray-tracing calculations are easily obtained from Eqs. (27) and (31) by application of the chain rule for differentiation.

3.4. O-X-B ray-tracing

The rays are launched from the plasma boundary at the position $(r,\theta,\phi) = (a,\theta_o,\phi_o)$ in a direction characterized by two angles χ and ψ as shown in Fig. 13.

χ and ψ are measured in a right-handed Cartesian coordinate system $(-\hat{r},\hat{\theta},\hat{\phi})$ connected to the launching point. χ is the angle between $\underline{N}$ and $\hat{\phi}$, and ψ is the angle measured from the $-\hat{r}\hat{\phi}$-plane to the $\underline{N}\hat{\phi}$-plane. χ and ψ play, respectively, the same role in the $(-\hat{r},\hat{\theta},\hat{\phi})$ system as the spherical coordinates θ and ϕ do in a $(\hat{x},\hat{y},\hat{z})$ system.

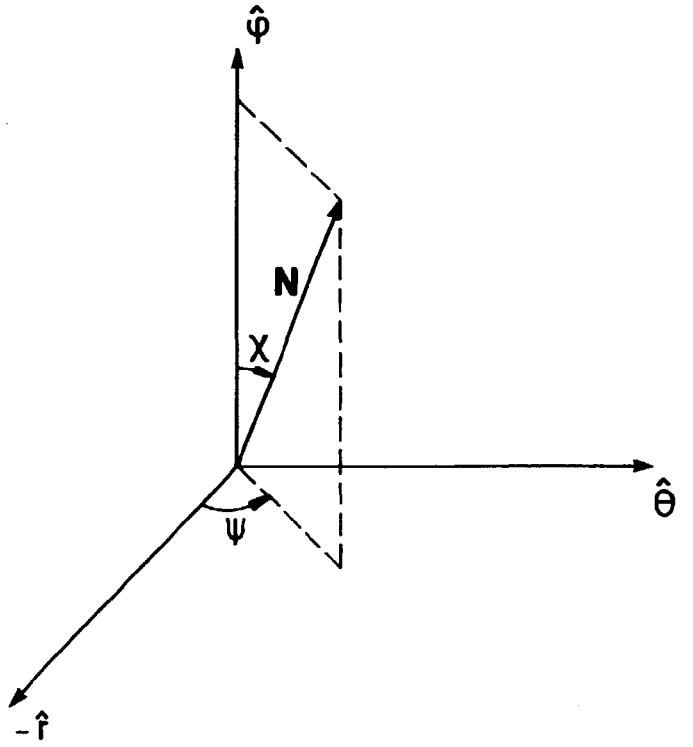

Fig. 13. Definition of the injection angles χ and ψ.

The rays are launched as O-waves defined by the plus sign in Eq. (18) and they are traced by solving the ray equations with the initial values

$$\underline{r}(0) = \begin{pmatrix} (R+a\cos\theta_o)\cos\phi_o \\ (R+a\cos\theta_o)\sin\phi_o \\ a\sin\theta_o \end{pmatrix} \tag{32}$$

and

$$\underline{N}(0) = \begin{pmatrix} \cos\theta_o\cos\phi_o & -\sin\theta_o\cos\phi_o & -\sin\phi_o \\ \cos\theta_o\sin\phi_o & -\sin\theta_o\sin\phi_o & \cos\phi_o \\ \sin\theta_o & \cos\theta_o & 0 \end{pmatrix} \cdot \begin{pmatrix} -\sin\chi\cos\psi \\ \sin\chi\sin\psi \\ \cos\chi \end{pmatrix} \tag{33}$$

Since $\underline{N}(0)$ is a unit vector, and $X = 0$ at $\underline{r}(0)$, it may be realized that the initial values $\underline{N}(0)$ and $\underline{r}(0)$ indeed satisfy the condition (17).

The cold dispersion function with the plus sign in front of Γ is used until the rays are close to the conversion point, defined as the position where the value $|N_r|$, the numerical value of the r-component of the refractive index vector, becomes less than $5 \cdot 10^{-3}$. The continuation of the rays on the X-wave branch of the dispersion function is insensitive to this value. At the conversion point the O-X conversion efficiency is evaluated by use of Eq. (10). The values of N_y and N_z in Eq. (10) are the y- and z-components of $\underline{N}$ in a local coordinate system with $\hat{x}$ in the $-\hat{r}$ direction, i.e the same direction as the density gradient, and $\hat{z}$ in the direction of $\underline{B}$. The values of L_n, Y and $N_{z,opt}$ in Eq. (10) are also evaluated at the actual conversion point.

Before the ray-tracing can continue on the other side of the conversion point, we must once more satisfy the initial condition in Eq. (17), i.e. we must ensure that the dispersion relation is satisfied for the newly created X-waves. First of all the sign in front of the factor Γ in the cold dispersion function must be set as negative. If the injected waves are not far from being optimal for mode conversion, the evanescent region is narrow, and this region is well described by a plasma slab identical to the one used to discuss the fundamental physics of the O-X-B scheme. In this case the density variation is along $\hat{r}$, and we may therefore assume that N_θ and N_ϕ remain constant across the region of evanescense. On the other hand, N_r must undergo a change of sign upon traversing the evanescent region to ensure that the r-component of the group velocity is maintained after the conversion. Therefore, if $\underline{N} = (N_r, N_\theta, N_\phi)$ is the value of $\underline{N}$ prior to the O-X-conversion, the point in space where the X-wave ray-tracing should start is found by setting $\underline{N} = (-N_r, N_\theta, N_\phi)$ and searching inwardly towards the plasma centre until the cold dispersion relation for the X-mode is satisfied.

The cold dispersion function is used for the X-wave until it passes through the plasma cut-off layer on its way away from the plasma centre and towards the upper hybrid resonance layer. At this point we switch to the hot dispersion function which is used for the rest of the calculations. As mentioned previously, no special action has to be taken in order to start the B-waves

at the upper hybrid resonance layer, since there is a smooth transition between the electromagnetic and the electrostatic dispersion branches of the hot dispersion function for the plasma parameter values of interest to us.

4. PROFILE CALCULATIONS

In order to judge the effectiveness of the O-X-B mode conversion scheme with respect to central and localized heating, we must determine the spatial deposition of the injected power. In this section we outline the methods used for calculating the spatial distributions of the absorbed wave power and the generated wave-driven current. At first we consider the spatial distributions due to power injected in a single direction, corresponding to a single ray; finally, a method to determine the spatial distributions of power and current due to an antenna having a finite spread of power, is outlined.

4.1. Radial power density profiles

In order to determine the spatial distribution of the absorbed wave power and the non-inductive wave-driven current it is necessary to calculate the absorption along the rays. The wave power, P(t), along a ray trajectory is given by

$$P(t) = P(0)\exp[-\tau(t)] \tag{34}$$

where P(0) is the initial power input and $\tau(t)$ the optical depth calculated as $\tau(t) = 2\int \underline{k}_i \cdot d\underline{r}$ along the ray where $\underline{k}_i$ is the imaginary part of the wave vector. As mentioned in Section 3.1, the ray equations are solved using only the Hermitian part of the dielectric tensor, so both $\underline{r}$ and $\underline{k}$ remain real along the whole ray trajectory. As long as the imaginary part of the wave vector is small compared to the real part we may, however, estimate $\underline{k}_i$

by Taylor expansion of the dispersion function for a homogenous plasma. This leads to the following expression for the optical depth

$$\tau(t) = \int_0^t \mathrm{Im}(D)/\mathrm{Re}(\partial D/\partial\omega)dt', \qquad (35)$$

which is used in Eq. (34) for calculating the wave power along the ray trajectories.

We assume that the heat transport in toroidal and poloidal directions is taking place on a much more rapid time scale than heat transport in the radial direction. In other words, we assume that the wave power is smeared out almost instantaneously on the nested magnetic flux surfaces surrounding the plasma centre. This assumption makes the absorption profile a function of radius only.

To obtain the radial power density profile for one ray we divide the torus into a number of nested shells with equal thickness. The power density, P_d, at the position of a given shell is then given by $P_d = \Delta P/\Delta V$, where $\Delta V = 2\pi R\pi(r_1^2-r_2^2)$ is the volume of the shell limited by the radial positions r_1 and r_2, and ΔP is the power absorbed between r_1 and r_2. If a ray crosses the same shell more than once, the individual contributions to the power density must of course be added.

4.2. Radial current density profiles

As shown by FISCH and BOOZER (1980), the wave damping is accompanied by a non-inductive toroidal current due to the creation of an asymmetric plasma resistivity arising from a reduced collision frequency of the heated electrons. The relation between the wave-driven current density, J, and dissipated wave power, P_d, is given by

$$J = -P_d \frac{e}{m_e v_{te} \nu_o} \frac{\hat{s}\cdot\nabla_v(wu^3)}{\hat{s}\cdot\nabla_v u^2} \frac{4}{5+Z_i} \tag{36}$$

where $\nu_o = \omega_{pe}^4 \ln\Lambda / 2\pi n v_{te}^3$ is the electron-ion collision frequency, $\ln\Lambda$ being the Coulomb logarithm. Z_i is the ion charge number ($Z_i = 1$ for the results presented in this work), $u = v/v_{te}$ and $w = v_z/v_{te}$, where v_z is the component of the velocity, $\underline{v}$, along the magnetic field lines, for the resonant electrons. Finally, $\hat{s}$ is a unit vector in the direction of which the electrons are displaced due to the wave damping, i.e. $\hat{s}$ is perpendicular to the magnetic field in the case of cyclotron absorption. By carrying out the differentiation in Eq. (36), and by assuming that the perpendicular component of $\underline{v}$ is negligible compared with v_z (v_z is 2 to 4 times v_{te} for the cases presented in this work) we find that

$$J = -P_d \frac{e}{m_e v_{te} \nu_o} \frac{3}{2} \frac{v_z^2}{v_{te}^2} \frac{|v_z|}{v_z} \frac{4}{5+Z_i} \tag{37}$$

The value of v_z/v_{te} in Eq. (37) is found from the resonance condition $\omega = \ell\omega_{ce} + k_z v_z$ with $\ell = 1$. It is obvious that by changing the sign of k_z a current will flow in the opposite direction, simply affirming that a reversal of the wave propagation direction reverses the current drive direction.

Since the wave power is assumed to be distributed uniformly within the toroidal shells, the current density profile is, like the power density profile, a function of radius only. As in the case of the power density profile, multiple contributions to the current density profile must be added.

4.3. Antenna modelling

Up to now we have discussed the radial power density and current density profiles belonging to a single ray. This corresponds to

the profiles for an antenna radiating its power within an infinitely narrow beam. However, our aim is to model a real antenna with a finite angular spread of power. This is done by considering a number of rays launched in different directions, each weighted according to the amount of power flowing from the antenna in the direction of the ray.

In the profile calculations we assume a Gaussian antenna radiation pattern of the form

$$S_{r_a}(r_a,\theta_a,\phi_a) = \begin{cases} \dfrac{P_o}{2\pi\sigma_o^2 r_a^2 \cos^3\theta_a} \exp\left(\dfrac{-\tan^2\theta_a}{2\sigma_o^2}\right) & \text{for } 0 \le \theta_a < \pi/2 \\ 0 & \text{for } \theta_a > \pi/2 \end{cases} \tag{38}$$

where r_a, θ_a and ϕ_a are ordinary spherical coordinates in a rectangular Cartesian coordinate system $(\hat{x}_a,\hat{y}_a,\hat{z}_a)$. The subscript a (antenna) is used in order to avoid confusion with the toroidal and the global coordinate systems defined in the previous section. The antenna is located at the origo of the coordinate system and the power is transmitted radially outwards, so both the θ_a and ϕ_a-components of the Poynting vector, $\underline{S}$, vanish. In Eq. (38) P_o is the total power radiated from the antenna. The divergence of the beam is specified through the quantity σ_o, which is related to beam angle, $\theta_{1/2}$, i.e. the angle within which half of the total power flowing from the antenna is radiated in the following way

$$\sigma_o = \tan(\theta_{1/2})/(2\ln 2)^{1/2} \tag{39}$$

The orientation of the antenna coordinate system relative to the toroidal coordinate system $(\hat{r},\hat{\theta},\hat{\theta})$ is shown in Fig. 14.

Three parameters are necessary to specify the orientation of the antenna. The beam direction $(\hat{z}_a)$ is defined by the angles χ_o and ψ_o, in exactly the same way as the initial ray direction is defined by the angles χ and ψ in the previous section. Furthermore, we allow the antenna coordinate system to be rotated an angle ξ_o around the $\hat{z}_a$-axis, away from the $-\hat{r}^{\vartheta}$-plane as shown in

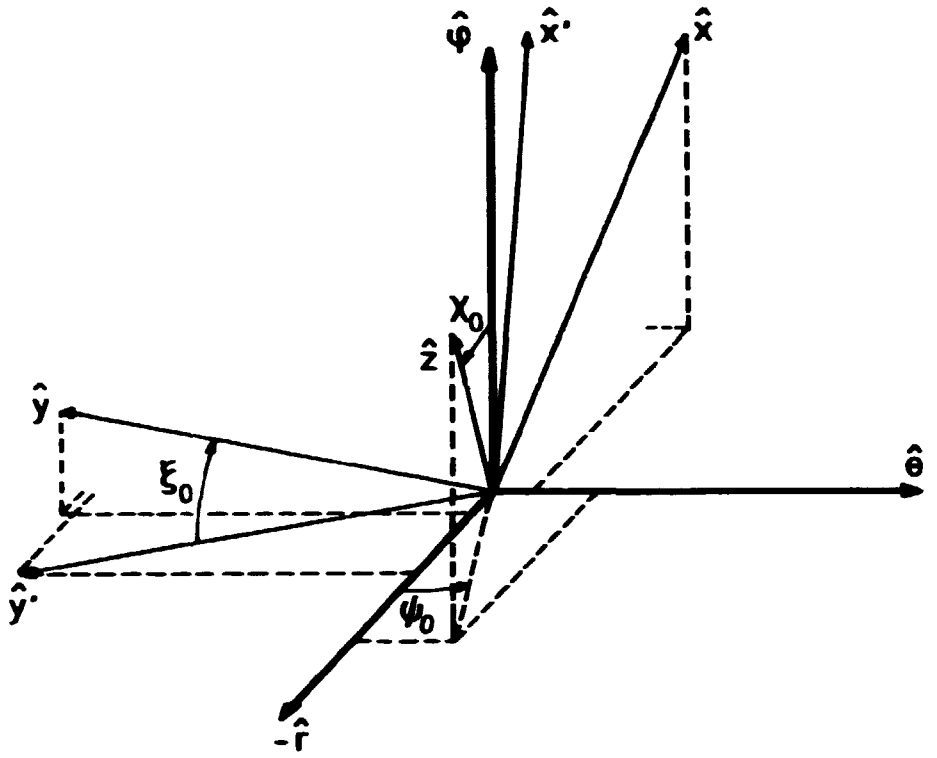

Fig. 14. Orientation of the antenna coordinate system $(\hat{x}_a,\hat{y}_a,\hat{z}_a)$, relative to the toroidal coordinate system $(\hat{r},\hat{\theta},\hat{\phi})$ defined in Fig. 12.

Fig. 14. For the radiation pattern in Eq. (38) this is, however, of no importance, since $\underline{S}$ does not depend on ϕ_a.

For the O-X-B mode conversion scheme it is crucial that the antenna beam be narrow. We may therefore assume that the beam hits only a small spot on the plasma surface, and all the rays used to model the antenna can be launched from the same point on the plasma boundary. However, to take the divergence of the beam into account, the rays must be sent out in different directions, each ray representing a small range of propagation directions.

In order to select the rays used to model an antenna, we divide a part of the $\chi\psi$-plane around (χ_0,ψ_0) into $(m-1)(n-1)$ similar rectangles as shown in Fig. 15.

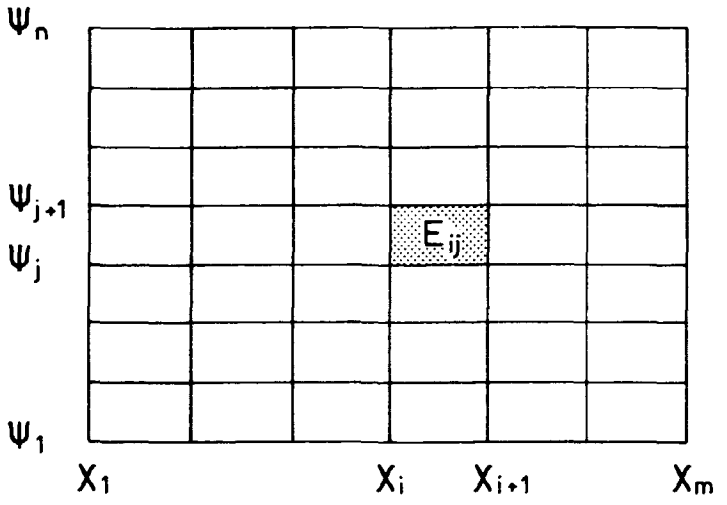

Fig. 15. The section of the $\chi\psi$-plane around the beam direction $(\chi,\psi) = (\chi_o,\psi_o)$ from which the rays used to model the antenna are launched.

Each rectangle corresponds to a small range of propagation directions, and a ray launched with $(\chi,\psi) = ([\chi_i+\chi_{i+1}]/2, [\psi_j+\psi_{j+1}]/2)$ represents the range of directions with $\chi_i < \chi < \chi_{i+1}$ and $\psi_j < \psi < \psi_{j+1}$ corresponding to the shaded area labelled E_{ij} on Fig. 15. This ray must be weighted according to the amount of power from the antenna flowing through E_{ij}. If w_{ij} denotes this amount of power, then P(0) in Eq. (34) must be put equal to w_{ij} for the individual rays, and the total radial profiles for the antenna are obtained by adding all the contributions to the profiles from the individual rays. However, when performing the ray-tracing calculations the actual radiation pattern is in fact disregarded, and all the rays are weighted equally, i.e. P(0) = 1 for all the rays. Later on, when all the rays are traced, we may then choose a specific antenna radiation pattern and weight the results accordingly. The total radial power density and current density profiles are then given by

$$P(r) = \sum_{i=1}^{m} \sum_{j=1}^{n} w_{ij} \tilde{P}_{ij}(r) \tag{40}$$

and

$$J(r) = \sum_{i=1}^{m} \sum_{j=1}^{n} w_{ij} \tilde{J}_{ij}(r) \tag{41}$$

where $\tilde{P}_{ij}(r)$ and $\tilde{J}_{ij}(r)$ are, respectively the radial power density profile and the radial current density profile for the individual rays; both normalized with respect to the actual power unit.

The outlined method for selecting and weighting the rays is particularly advantageous when the ray-tracing calculations are time consuming, because the same set of rays may be used to model several antenna radiation patterns. As a disadvantage one needs to store all results concerning power absorption and wave-driven current for all rays, in order to calculate the profiles.

Finally, a procedure for calculating the weights, w_{ij}, is given. The amount of power from the antenna flowing through E_{ij} may be calculated as the flux of $\underline{S}$ through U_{ij}, the part of the unit sphere surrounding the antenna, corresponding to E_{ij}, i.e.

$$w_{ij} = \int_{U_{ij}} S_{r_a}(x_a, y_a, z_a) d\Omega \tag{42}$$

The surface integral in Eq. (42) may be transformed to a plane integral of the form

$$w_{ij} = \int_{\chi_i}^{\chi_{i+1}} \left[\int_{\psi_j}^{\psi_{j+1}} S_{r_a}(\underline{r}_a(\chi,\psi)) \left| \frac{\partial \underline{r}_a}{\partial \chi} \times \frac{\partial \underline{r}_a}{\partial \psi} \right| d\psi \right] d\chi \tag{43}$$

where $\underline{r}_a(\chi,\psi) = (x_a(\chi,\psi), y_a(\chi,\psi), z_a(\chi,\psi))$ specifies how x_a, y_a and z_a on the unit sphere depend on χ and ψ. In order to determine this dependence, we need to determine the connection between the unit base vectors in the antenna and the toroidal co-

ordinate systems. This is given by

$$\begin{pmatrix} \hat{x}_a \\ \hat{y}_a \\ \hat{z}_a \end{pmatrix} = \underline{\underline{J}}_2 \begin{pmatrix} \hat{r} \\ \hat{\theta} \\ \hat{\phi} \end{pmatrix}$$

with

$$\underline{\underline{J}}_2 = \begin{pmatrix} \cos\xi_o & -\sin\xi_o & 0 \\ \sin\xi_o & \cos\xi_o & 0 \\ 0 & 0 & 1 \end{pmatrix} \cdot \begin{pmatrix} \cos\chi_o\cos\psi_o & -\cos\chi_o\sin\psi_o & \sin\chi_o \\ -\sin\psi_o & -\cos\psi_0 & 0 \\ -\sin\chi_o\cos\psi_o & \sin\chi_o\sin\psi_o & \cos\chi_o \end{pmatrix}$$

A unit vector, $\underline{N}$, in the antenna coordinate system is given by

$$\underline{N} = \sin\theta_a\cos\phi_a\hat{x}_a + \sin\theta_a\sin\phi_a\hat{y}_a + \cos\theta_a\hat{z}_a \tag{44}$$

and one in the toroidal coordinate system is given by

$$\underline{N} = -\sin\chi\cos\psi\hat{r} + \sin\chi\sin\psi\hat{\theta} + \cos\chi\hat{\phi} \tag{45}$$

By equating the expressions for $\underline{N}$ in Eqs. (44) and (45) one obtains

$$\begin{pmatrix} x_a \\ y_a \\ z_a \end{pmatrix} = \begin{pmatrix} \sin\theta_a\cos\phi_a \\ \sin\theta_a\sin\phi_a \\ \cos\theta_a \end{pmatrix} = \underline{\underline{J}}_2 \begin{pmatrix} -\sin\chi\cos\psi \\ \sin\chi\sin\psi \\ \cos\chi \end{pmatrix}$$

which is the desired connection between x_a, y_a and z_a on the unit sphere and χ and ψ.

Finally, the derivatives of $\underline{r}_a$ with respect to χ and ψ may be computed

$$\frac{\partial \underline{r}_a}{\partial \chi} = \underline{\underline{J}}_2 \begin{pmatrix} -\cos\chi\cos\psi \\ \cos\chi\sin\psi \\ -\sin\chi \end{pmatrix}$$

$$\frac{\partial \underline{r}_a}{\partial \psi} = \underline{\underline{J}}_2 \begin{pmatrix} \sin\chi\sin\psi \\ \sin\chi\cos\psi \\ 0 \end{pmatrix}$$

and the weights can be obtained from Eq. (43) by use of a numerical method for calculating plane integrals.

5. NUMERICAL RESULTS

In this section some numerical results obtained by CONRAY are presented. The examples are related to the Danish DANTE tokamak and the Princeton PLT tokamak. Unless otherwise stated the parameters used by CONRAY for the two machines are the ones listed in Table 1.

Table 1. Parameters for DANTE and PLT used by CONRAY.

Parameter	Symbol	Unit	DANTE	PLT
Major radius	R	[m]	0.50	1.32
Minor radius	a	[m]	0.11	0.40
Central plasma density	n(0)	[m^{-3}]	$1 \cdot 10^{19}$	$6 \cdot 10^{19}$
Toroidal field on axis	$B_\phi(0)$	[T]	0.625	2.14
Safety factor at centre	q(0)		1	1
Safety factor at surface	q(a)		3	4
Central electron temperature	$T_e(0)$	[keV]	0.2	1.0
Wave frequency	f	[GHz]	17.5	60.0
Beam angle	$\theta_{1/2}$	[deg.]	15.0	1.5
Optimal horizontal angle	χ_o	[deg.]	49	53
Optimal vertical angle	ψ_o	[deg.]	3.2	2.2
Total power input	P_o	[kW]	20	1000

Figure 16 shows the ray trajectories along with the wave power (normalized to 1 at the plasma boundary) for the rays injected at optimal angles $(\chi,\psi) = (\chi_o,\psi_o)$ in DANTE and PLT. The rays shown are projected onto the toroidal plane and a poloidal plane following the rays.

In both cases shown, the wave frequency is chosen to match the electron cyclotron frequency at the plasma centre. The rays injected as O-waves are fully converted into X-waves near the plasma cut-off. The X-waves propagate towards the upper hybrid resonance layer, where they become increasingly electrostatic, and thus transformed into Bernstein waves. The B-waves move towards the centre of the plasma, and the ray trajectories tend to become more and more parallel with the toroidal magnetic field lines. Along the trajectories for the B-waves, the wave vector is almost perpendicular to the ray trajectory, inferring the absence of significant damping away from the electron cyclotron resonance. From the figure it is seen that the B-waves are damped in a narrow radial region near the cyclotron resonance. Even though the damping seems to be very sudden, it actually occurs over many wavelengths as will be demonstrated. The damping simply seems abrupt because the rays move very little in the radial direction near the magnetic axis where the absorption takes place.

The central ray for DANTE differs from the one for PLT by reversing its toroidal propagation direction close to the magnetic axis. This effect is due to the presence of the poloidal magnetic field.

The reversal of the propagation direction has also been observed for rays launched in directions other than the optimal, and even rays that reverse several times have been found. Due to the reversals the power may be absorbed in two or more separate radial regions and this could give rise to multiply humped power deposition profiles. The reversal of the propagation direction is accompanied by a change of sign of the parallel part of the wave vector. As mentioned in Section 4.2, a reversal of the propagation direction reverses the current drive direction, so multiply humped power deposition profiles have a negative influence on

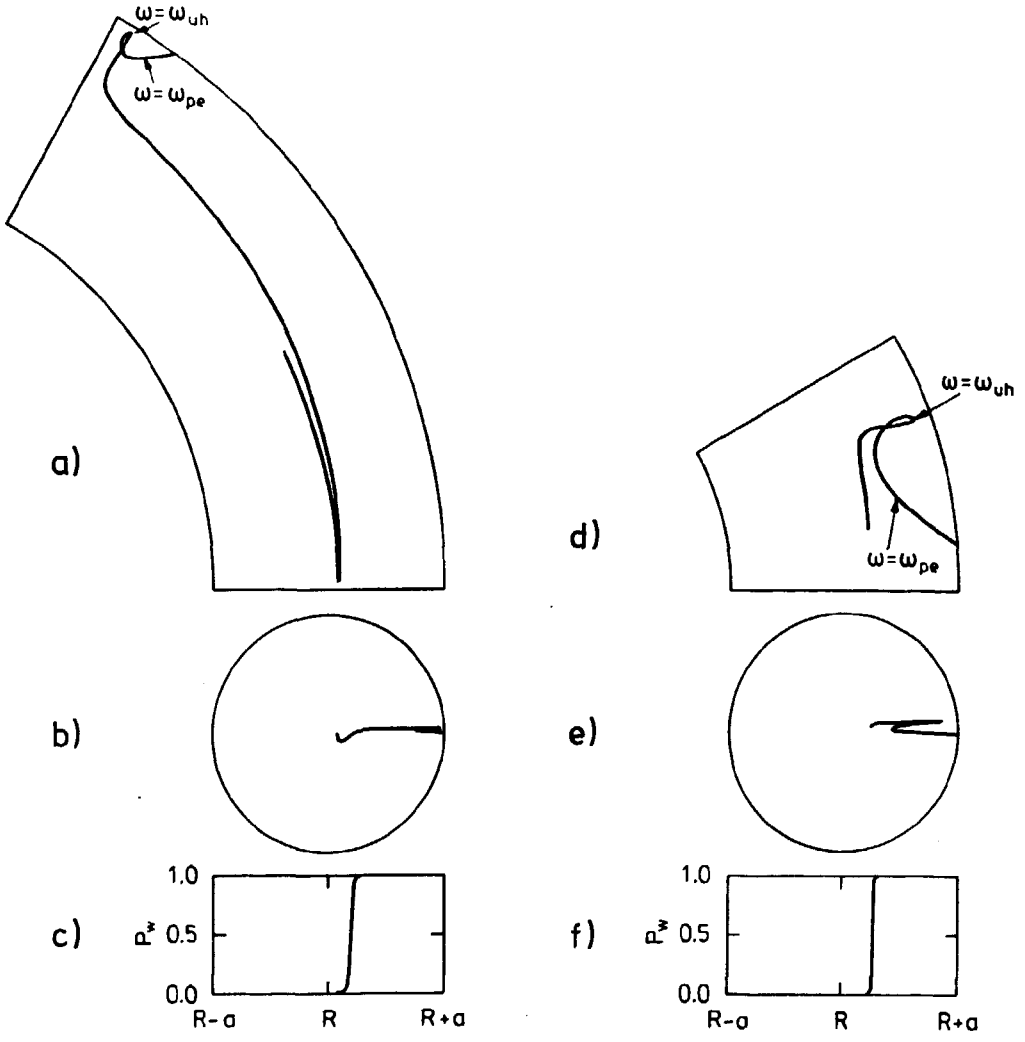

Fig. 16. Rays injected at optimal angles $(\chi,\psi) = (\chi_o,\psi_o)$ in DANTE and PLT. The O-X and X-B mode conversion points are indicated by $\omega = \omega_{pe}$ and $\omega = \omega_{uh}$, respectively. (a) Toroidal projecion of the optimal ray for DANTE; (b) Poloidal projection of the optimal ray for DANTE; (c) Non-absorbed fraction of the incident wave power as function of the distance to the centre line of the torus for the optimal ray in DANTE; (d) Same as (a) for PLT; (e) Same as (b) for PLT; (f) Same as (c) for PLT.

the total current driven by the waves. On the other hand, the possibility of driving currents in opposite directions within a narrow radial region can be used to shape the total current profile. A somewhat more detailed investigation of this problem is reported elsewhere (HANSEN, LYNOV and MICHELSEN (1984)).

As may be seen from Appendix B, the equations expressing the right-hand sides of the ray equations are rather long and complex, and one might expect that even a single mistake in the equations could alter the ray paths drastically. A valuable check of the correctness of the numerical solution may be obtained by investigating the quantity $N_\phi(R+x)$ which, as mentioned in Section 2.5, must remain constant along the ray trajectory. In Fig. 17 the value of $N_\phi(R+x)$ as function of the ray length is shown for the optimal ray in DANTE.

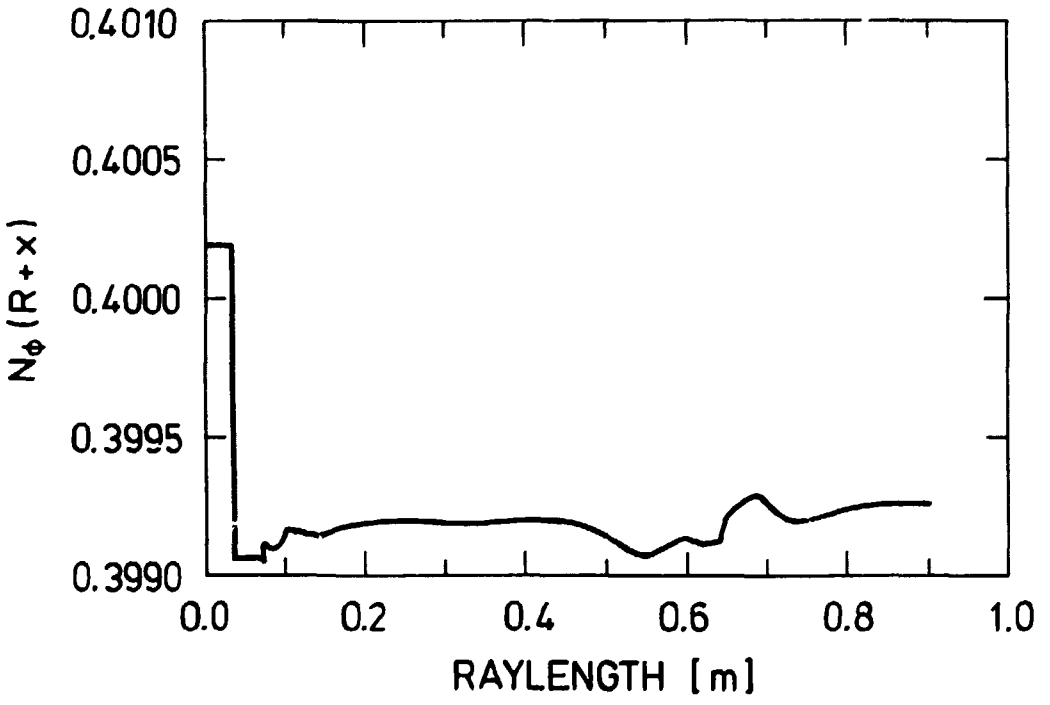

Fig. 17. $N_\phi(R+x)$ versus ray length for the optimal ray in DANTE.

Besides a minor drop in the value of $N_\phi(R+x)$ at the O-X conversion point due to the small jump in radial direction where N_ϕ was kept fixed, $N_\phi(R+x)$ remains approximately constant along the whole ray path, and this result seems to support the correctness of the numerical solution.

In Fig. 18 we show the variation of the toroidal angles θ and ϕ along the ray path, for the optimal ray in DANTE.

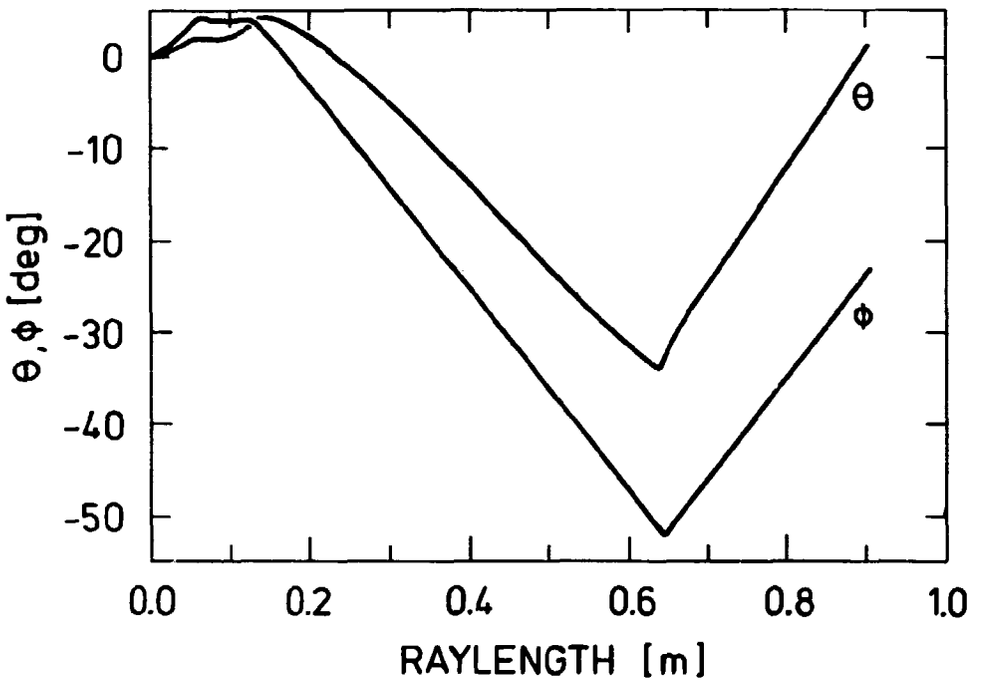

Fig. 18. θ and ϕ versus ray length for the optimal ray in DANTE.

From the figure it is seen that a reversal of the group velocity in toroidal direction of the Bernstein waves takes place after a ray length of approximately 0.64 m. At this point a reversal in poloidal direction is also seen to take place.

Figure 19 shows the r, θ and ϕ-components of the refractive index vector along the optimal ray in DANTE.

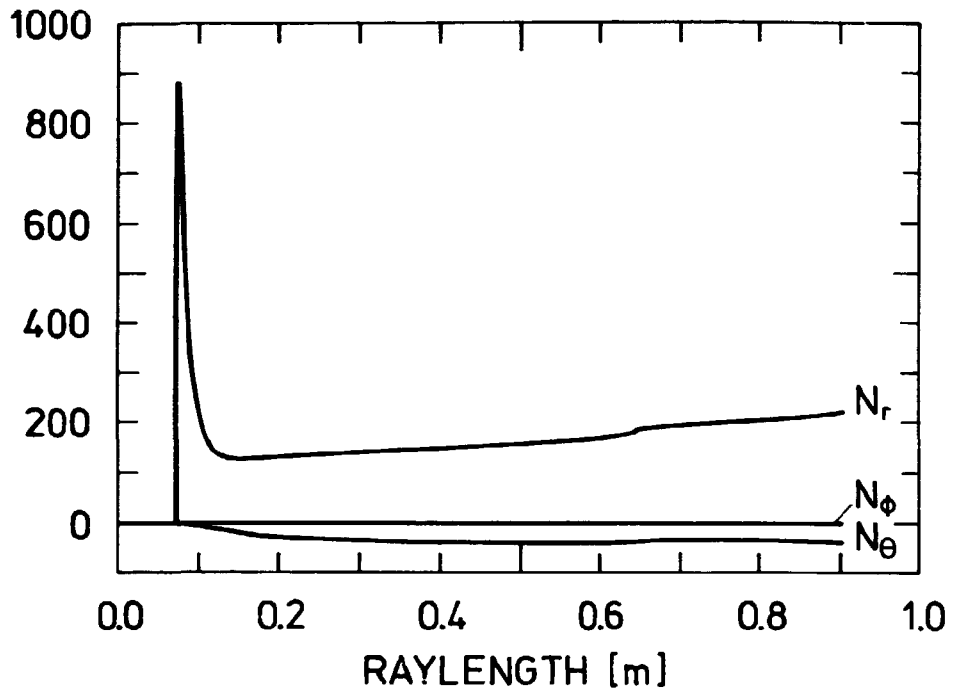

Fig. 19. The r, θ and ϕ-components, N_r, N_θ and N_ϕ, of the refractive index vector for the optimal ray in DANTE.

We see that the r-component of $\underline{N}$ is by far the most dominant along most of the ray trajectory. On a very short distance close to the upper hybrid resonance layer N_r increases drastically and reaches a value of almost 900 corresponding to a wavelength of 0.02 mm. After the upper hybrid layer N_r decreases to a level slightly below 200, corresponding to a wavelength of 0.1 mm.

In Fig. 20 we show P_w, the non-absorbed wave power relative to the initial power input as function of the ray length, for the optimal ray in DANTE.

The major fraction of the absorbed power is delivered by the Bernstein waves to the plasma over a length of approximately 0.25 m just prior to the reversal of the ray. Since the wavelength of the Bernstein waves is very much shorter than the length over which the damping takes place, the assumption of weak

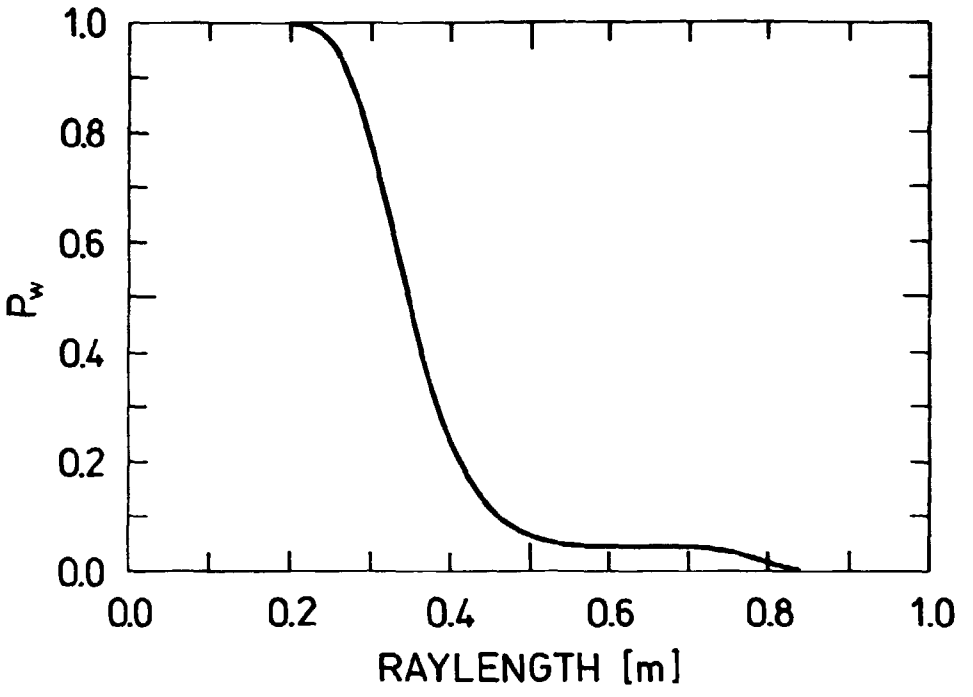

Fig. 20. The fractional non-absorbed wave power versus ray length for the optimal ray in DANTE.

damping indeed holds good, and the assumption under which the optical depth in Eq. (35) is derived is satisfied. The remaining approximately 5 per cent of the injected power is absorbed after the reversal of the Bernstein waves, and again over a long distance compared to the wavelength.

In Fig. 21 we show the ratio of the group velocity to the velocity of light in vacuum, $v_g/c = |d\underline{r}/dt|/c$, as function of the ray length for the optimal ray in DANTE.

The value of v_g/c decreases from 1 to almost 0 at the upper hybrid resonance layer, where the ray loops, and v_g/c remains very small along the part of the ray trajectory corresponding to the Bernstein waves moving in radial direction. After the Bernstein waves start to move in the toroidal direction v_g/c increases to a level of approximately 2 per cent of the initial value. At the point of reversal the value of v_g/c becomes once more very small.

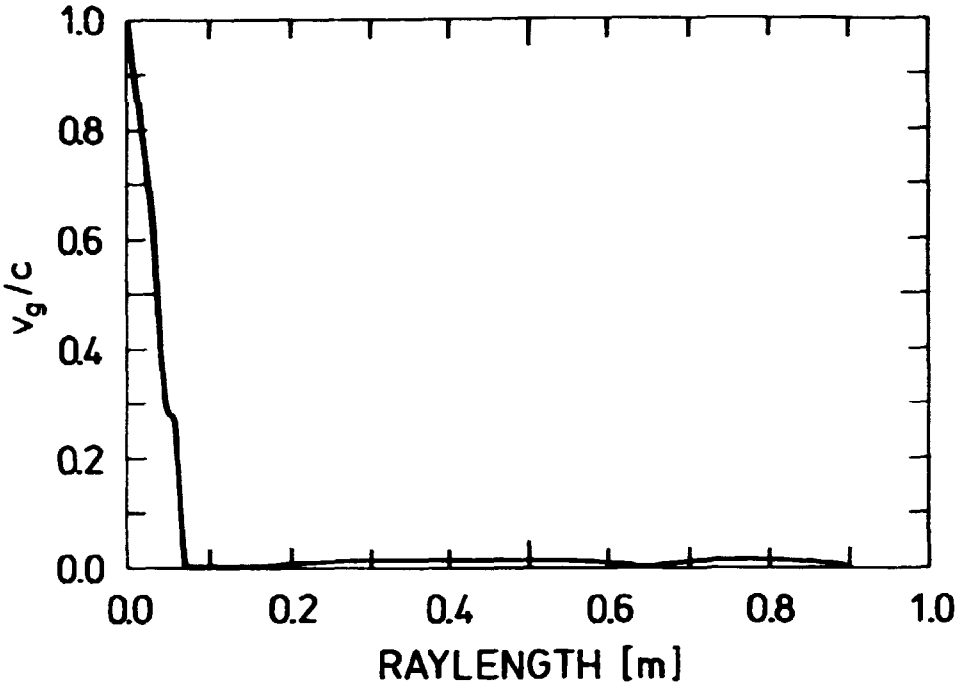

Fig. 21. The group velocity $v_g = |d\underline{r}/dt|$ normalized with the velocity of light as function the ray length.

We have investigated how the power transmission coefficient, T, depends on the injection angles χ and ψ. The rays launched on the ordinary branch are traced up to the conversion point where the power transmission coefficient is evaluated as described in Section 3.4. The results for the two machines are shown in Fig. 22.

The optimal angles for DANTE are seen to be $(\chi_o, \psi_o) = (49^o, 3.2^o)$ and the same numbers for PLT are $(\chi_o, \psi_o) = (53^o, 2.2^o)$. Furthermore, it is seen that the 50 per cent power transmission contour lies within an angle of approximately 1^o away from the optimal angles in the case of PLT, and approximately 8^o away from the optimal angles in the case of DANTE. This is in good agreement with the results for the transmission coefficient obtained in Section 2.5, for the simple toroidal plasma equilibrium. For small angles, ψ, corresponds θ in Fig. 11 roughly to χ in Fig. 22, and the curves in Fig. 11 which are also based on parameters

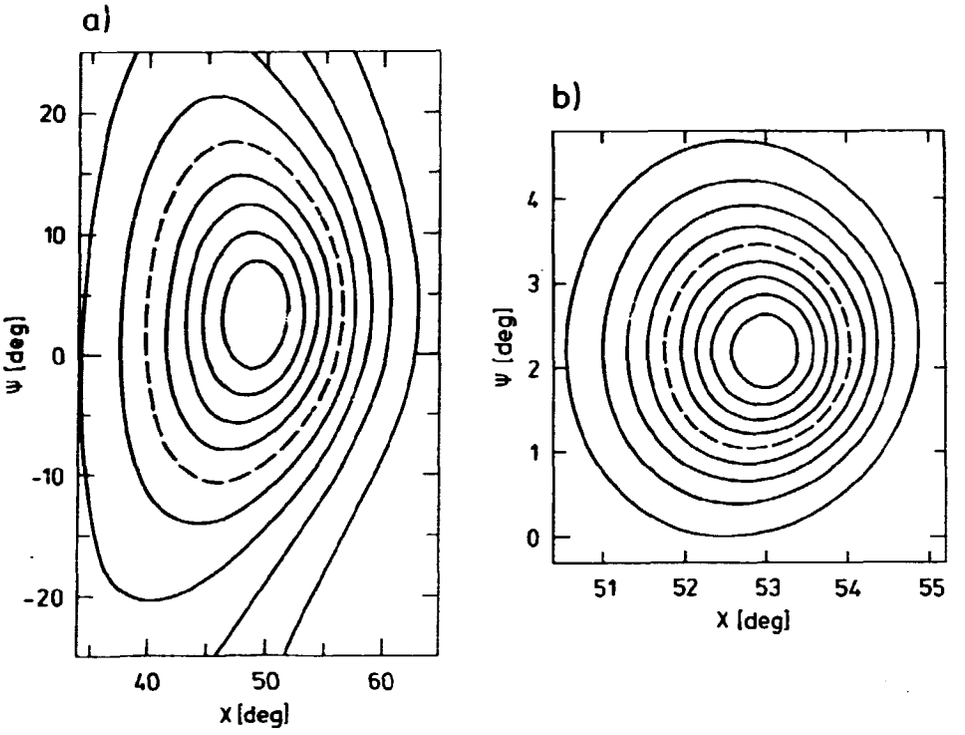

Fig. 22. The power transmission coefficient, T, for the O-X mode conversion as function of the injection angles χ and ψ. The contours represent 10 per cent levels of T. The 50 per cent power transmission contours are indicated by the dashed curves. (a) Parameters relevant to DANTE; (b) Parameters relevant to PLT.

for PLT and DANTE gives respectively 1^{o} and 7^{o} for the half widths at 50 per cent O-X power transmission.

In order to investigate whether or not the optimal injection angles are critically dependent on changes in the density or magnetic field we have plotted χ_o and ψ_o versus X(0) for different values of Y(0). The results are shown in Fig. 23.

It is seen that for large values of the central density, both χ_o and ψ_o are almost independent of the central density, whereas for densities slightly above the critical density, the optimal angles become more density dependent. For central densities above 1.5 times the critical density the variation of χ_o and ψ_o is well

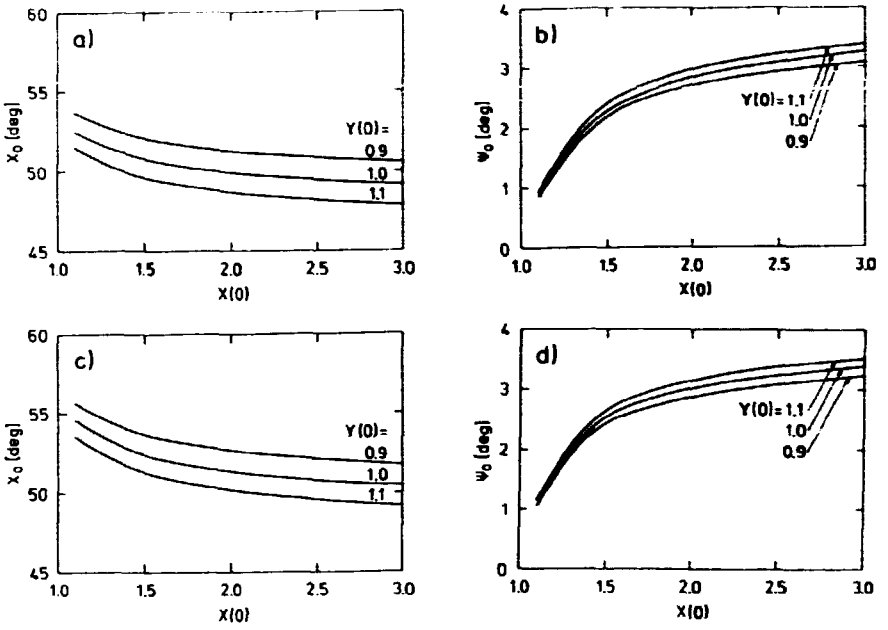

Fig. 23. The optimal angles χ_o and ψ_o versus central density for for different values of Y(0). (a) The optimal angle χ_o in DANTE; (b) The optimal angle ψ_o in DANTE; (c) Same as (a) with parameters relevant to PLT; (d) Same as (b) with parameters relevant to PLT.

well below 1^o, even for large variations of the central density. It is also seen that minor changes in the magnetic field intensity have only a slight effect on the optimal angles.

Figure 24 shows the radial power deposition profiles and the associated radial current density profiles when the total antenna radiation patterns are taken into account. The antennae are assumed to have a Gaussian radiation pattern as the one described in Section 4.3, and to radiate with the optimal polarization for O-wave generation. When calculating the power and current density profiles, the individual rays are weighted according to the amount of power from the antenna flowing in the particular direction, and the O-X power transmission coefficient at the plasma cut-off layer. The results in Fig. 24 are based on a total of 255 rays for DANTE and 169 rays for PLT.

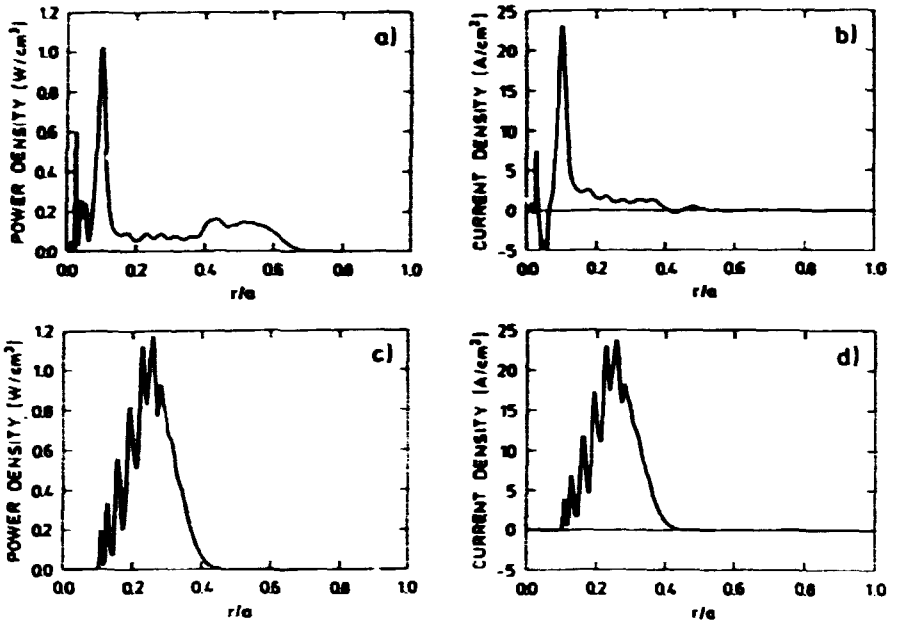

Fig. 24. Radial power density profiles and radial current density profiles for DANTE and PLT. (a) The radial power density profile for a total power input of 20 kW into DANTE; (b) The associated current density profile; (c) Same as (a) for a total power input of 1 MW into PLT; (c) The associated current density profile.

The profiles for DANTE are seen to be rather spiky close to the plasma centre. This is due to the finite number of rays used to model the antenna, and that the rays absorbed close to the electron cyclotron resonance layer propagate very little in radial direction during the period of absorption. The current drive profiles look qualitatively like the power density profiles. Notice, however, that the Bernstein waves drive the current in opposite directions close to the plasma centre, in the case of DANTE.

The total efficiency, i.e. the ratio of the power dissipated by the B-waves to the amount of power injected, is 29 per cent for DANTE and 33 per cent for PLT. After several reflections between the tokamak walls and the plasma much of the remaining power,

i.e. approximately 70 per cent, will eventually be delivered to the electrons in the outer region of the plasma by cyclotron damping (BARANOV et.al. (1983)). Naturally, by further collimation of the antenna beams, one could increase the total efficiency very much, thereby producing more localized heating.

The results show a much lower current drive efficiency by the electron Bernstein waves (5 mA/W for DANTE and 8mA/W for PLT), than by current drive with lower hybrid waves, where efficiencies in excess of 1 A/W have been demonstrated (BERNABEI et.al. (1983)).

From Fig. 24 it is seen that the power deposition profiles are peaked at some distance away from the magnetic axis toward the outside of the tokamak. By decreasing the ratio $\omega_{ce}(0)/\omega$ the profiles will tend to shift further towards the inside of the tokamak and produce heating closer to the plasma centre. We have investigated the effect of decreasing the ratio $\omega_{ce}(0)/\omega$ in more detail for the PLT device. The plasma parameters used for this investigation are the ones listed in Table 1, except that $n(0)$, the central density is $8 \cdot 10^{19}$ m^{-3}. We consider three different situations where the wave frequency takes the values 60 GHz, 65 GHz and 70 GHz, corresponding to a value of $\omega_{ce}(0)/\omega$ of 1.00, 0.921 and 0.856, respectively.

In order to determine the optimal angles and the beam angles for the antenna radiation patterns to be used for the three cases under consideration, the variation of the O-X transmission coefficient for varying injection angles χ_o and ψ_o is shown in Fig. 25.

The optimal angles (χ_0, ψ_0) for the three cases are seen to be $(54.9^o, 2.1^o)$ at f = 60 GHz, $(53.2^o, 2.5^o)$ at f = 65 GHz and $(51.6^o, 2.9^o)$ at f = 70 GHz. In the three cases the 50 per cent transmission contour lies, respectively, approximately 2^o, 1.7^o and 1.3^o away from the optimal angles, and these values are used for the antenna beam angle, $\theta_{1/2}$.

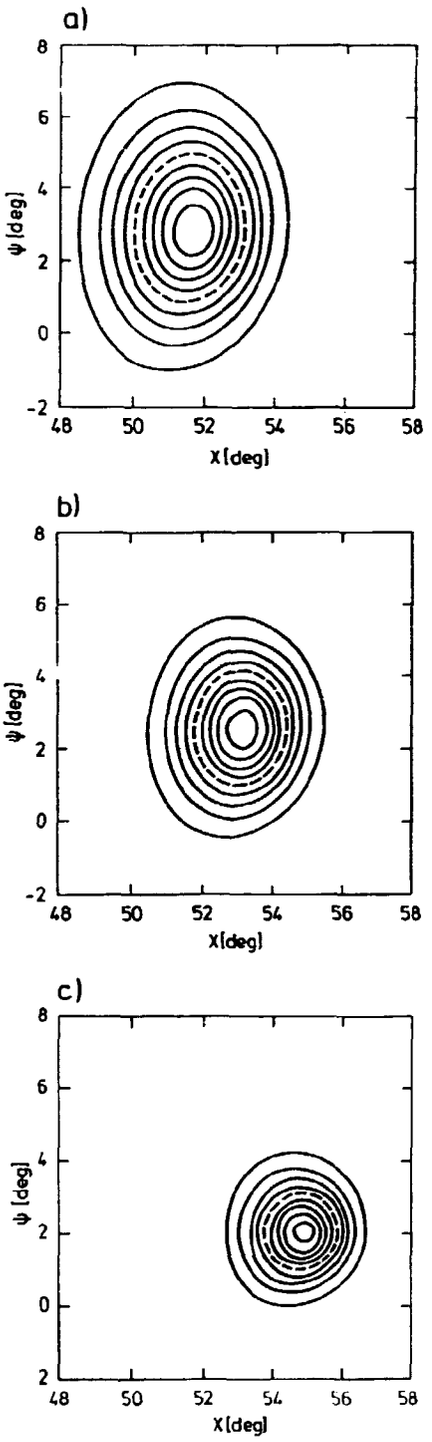

Fig. 25. The power transmission coefficient, T, for the O-X mode conversion as function of x_o and ψ_o in PLT. n(0) = $8 \cdot 10^{19}$ m^{-3}. (a) f = 60 GHz; (b) f = 65 GHz; (c) f = 70 GHz.

Each radial power density profile is based on a total of 169 rays, and in Fig. 26 we show in each case the ray trajectories of 16 selected rays launched equidistantly from the $\chi\psi$-plane around (χ_o, ψ_o)

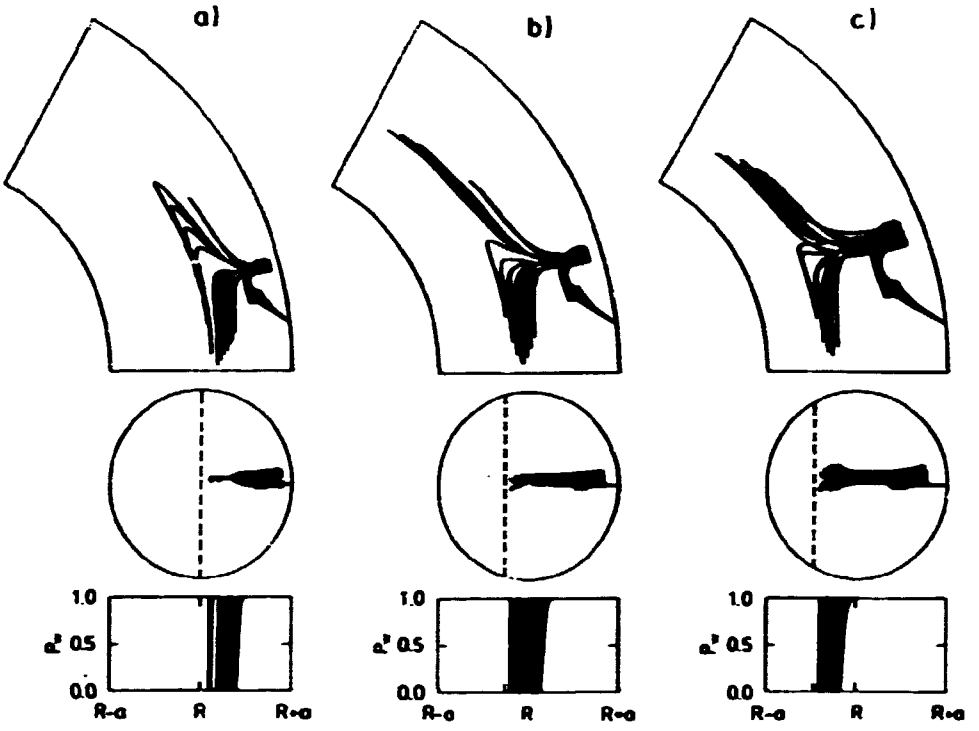

Fig. 26. Ray trajectories of 16 selected rays launched uniformly in the $\chi\psi$-plane around the optimal angles χ_o and ψ_o in PLT. The position of the electron cyclotron resonance layer in the poloidal plane is indicated by the dashed line. $n(0) = 8 \cdot 10^{19}$ m^{-3}. (a) f = 60 GHz, $(\chi_o, \psi_o) = (54.9^o, 2.1^o)$; (b) f = 65 GHz, $(\chi_o, \psi_o) = (53.2^o, 2.5^o)$; (c) f = 70 GHz, $(\chi_o, \psi_o) = (51.6^o, 2.9^o)$.

In the low-frequency case where the electron cyclotron resonance layer is located at the plasma centre the Bernstein waves are absorbed in a region slightly away from the centre towards the outside of the tokamak. Notice that in this case there is a tendency for the Bernstein waves to focus in the poloidal plane.

In the high-frequency case shown in Fig. 26c, where f = 70 GHz, the electron cyclotron resonance layer is shifted a distance of almost half a minor radius towards the inside of the tokamak. In this case one still observes heating off centre. However, in contrast to the low-frequency case the absorption takes place away from the centre towards the inside of the torus. Also in contrast to the low-frequency situation, the Bernstein waves diverge in the poloidal plane near the cyclotron resonance layer. This may be explained by the fact that the Bernstein waves in the latter case propagate towards lower densities, whereas in the first case they propagate towards higher densities.

Finally, in the intermediate case, where f = 65 GHz, the electron cyclotron resonance layer is shifted approximately a quarter of a minor radius towards the inside of the tokamak. From Fig. 26b it is seen that the Bernstein waves are absorbed around the magnetic axis, and $\omega_{ce}(0)/\omega = 0.921$ seems to be near the optimum choice for central heating for the PLT device.

In Fig. 27 we show the power density profiles for the three cases.

We see that the power is delivered very centrally in the machine in the medium-frequency case. In fact, almost all of the power carried by the Bernstein waves are absorbed within a distance of approximately a fifth of a minor radius away from the centre.

6. CONCLUSION

In the previous sections we have investigated various ECRH schemes for heating overdense plasmas, with particular emphasis on the O-X-B mode conversion scheme.

Results from ray-tracing calculations of the O-X-B heating scheme for parameters relevant to DANTE and PLT were presented in Sec-

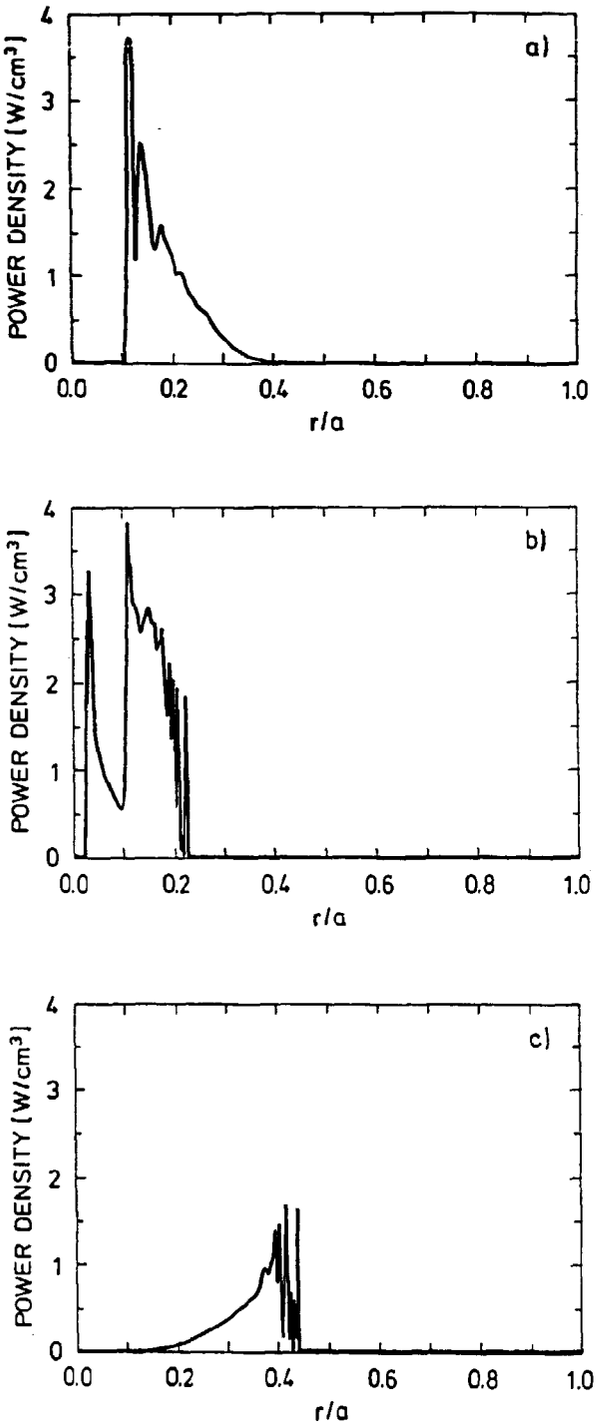

Fig. 27. Radial power density profiles for PLT. n(0) = $8 \cdot 10^{19}$ m^{-3}. (a) f = 60 GHz, $(\chi_o, \psi_o) = (54.9^o, 2.1^o)$; (b) f = 65 GHz, $(\chi_o, \psi_o) = (53.2^o, 2.5^o)$; (c) f = 70 GHz, $(\chi_o, \psi_o) = (51.6^o, 2.9^o)$.

tion 5. Power deposition and current density profiles due to absorption of electron Bernstein waves generated by realistic antenna radiation patterns were computed along with overall heating and current drive efficiencies. The effects of the antenna radiation patterns were simulated by tracing a large number of rays transmitted in different directions around the main beam direction. Each ray was weighted according to the amount of power from the antenna flowing in the direction of the ray. Furthermore, each ray was weighted according to the analytical O-X mode conversion efficiency at the mode conversion point.

Very high heating efficiencies can be obtained by the O-X-B scheme, but only if the antenna system satisfies certain requirements. In the first place, a large fraction of the radiation at the plasma boundary should be polarized in the O-mode. Secondly, the antenna beam width must be kept narrow in order to have an overall high O-X mode conversion efficiency, and finally the antenna beam must be injected near an optimal angle (typically 50°) to the magnetic field lines.

As demonstrated in Section 2.5 and Appendix A, the O-mode is elliptically polarized at the plasma boundary for waves propagating oblique to $\underline{B}$. A linearly polarized wave may have a power content as high as 35 per cent of the undesired X-mode at injection angles near the optimal for O-X mode conversion. Different schemes for generating electromagnetic waves with a specified elliptical polarization have been described by MOELLER et.al. (1983), BEYER et.al. (1983) and PRATER et.al. (1984).

The requirements to the narrowness of the beam are most severe on devices with high magnetic fields. For low-field tokamaks like DANTE, the full beam width at half power can be as large as 15° without a substantial loss of power to the reflected O-mode in the O-X mode conversion process. In a large high-field tokamak like NET/INTOR with $B(0) = 5.5$ T, $R = 5.2$ m, $a = 1.2$ m and $n(0) = 4 \cdot 10^{20}$ m^{-3} the full beam width should be less than 1°. Even though this requirement is severe, the decreasing wavelength and the possibility of increasing the dimensions of the antenna aperture with increasing magnetic field strength and tokamak dimen-

sions make it technically possible to meet the requirements to the narrowness of the beam. The requirements of the narowness of the beams are less severe when the O-X-B mode conversion scheme is used at the second harmonic of the electron cyclotron frequency. HSU et.al. (1983) found that the allowed beam width for efficient mode conversion at the second harmonic is enhanced by a factor of 1.5 over that of the fundamental. However, second harmonic O-X-B mode conversion requires that the central density exceeds the maximum density $n_{max} = \varepsilon_o B^2/m_e$ defined in Section 2.3 by a factor of more than 4.

In Section 5 we found that the optimal angles were rather insensitive to small changes in plasma density and magnetic field as long as the central density was more than 50 per cent higher than the critical density. However, although density fluctuations do not seriously affect the optimal injection angle, scattering of the rays by random density fluctuations will tend to increase the effective beam width thereby lowering the total O-X mode conversion efficiency. According to HUI et.al. (1981), density fluctuations as low as one per cent may cause noticeable scattering of ordinary waves propagating perpendicular to the magnetic field in a tokamak. A quantitative estimate requires further investigations as to how serious an effect wave scattering from density fluctuations has on the O-X-B scheme where the O-waves are injected obliquely to the magnetic field lines and where the O-waves have to travel only a fraction of the minor radius before reaching the O-X conversion region.

Another effect due to density fluctuations which could be important to the O-X-B scheme has been described by WILHELM et.al. (1984) referring to the ECRH experiments in the Wendelstein VII-A stellarator. The authors propose that density fluctuations near the upper hybrid layer scatter the B-waves, so that they obtain so large a wave number parallel to the magnetic field that they are totally absorbed at the upper hybrid layer and not near the cyclotron layer. We do not believe this effect to be very pronounced in a tokamak plasma since the measured values of the parallel wavelength of density fluctuations in tokamaks (see e.g.

SURKO and SLUSHER (1976)) are much too large to give noticeable scattering of the B-waves in the direction to the magnetic field.

When the frequency of the microwave radiation is chosen to be equal to the electron cyclotron frequency on the magnetic axis in the tokamak, the power density and current density profiles are peaked at some distance away from the centre. We have shown that central heating can be obtained by decreasing the ratio of $\omega_{ce}(0)$ to ω. In the case of PLT, an 8 per cent increase of the microwave frequency turned out to be the optimum choice for central heating.

It should be pointed out that the results are based on linearized equations describing the wave propagation and absorption and that the WKB assumption has been made. To the best of our knowledge, the question of nonlinear effects on the O-X mode conversion process is at present an open question. On the other hand, nonlinear effects in the X-B conversion process have been observed by MCDERMOTT et.al. (1982), where parametric decay of the X-wave into a lower hybrid wave and an electrostatic Bernstein wave were detected when the incident RF power exceeded a certain threshold. Heating of the ion distribution tail was also observed (WILHELM et.al. (1984)) near the upper hybrid resonance layer in the ECRH experiment in Wendelstein VII-A, indicating a similar process. An estimate of the importance of parametric decay in the O-X-B scheme requires a complex calculation of the electric field strength along a complicated ray paths, and this is not included in the present version of CONRAY.

As for the validity of the WKB assumption, the values of the parameter $k_o a$ which should be much larger than 1, are 500 in the case of PLT and 40 in the case of DANTE. In order to study the wave propagation without making the WKB assumption, numerical investigations have been initiated for the full wave problem in a slab geometry, and the first results which are computed for parameters relevant to the O-X conversion region in a cold plasma have been obtained (HANSEN, LYNOV, MAROLI and PETRILLO (1986)).

In conclusion, the numerical results indicate that the O-X-B mode conversion scheme should be considered seriously in connection with the application of ECRH to overdense plasmas. However, experimental investigations of the effectiveness of this scheme in a tokamak plasma are still to be performed.

ACKNOWLEDGEMENTS

The author wishes to thank the Association EURATOM-Risø National Laboratory for the scholarship. I thank my colleagues in the Fundamental Plasma Physics Group and the ECRH Group for their kindness and great help during my studies, and especially J.P. Lynov who gave me excellent support throughout the work.

REFERENCES

ABRAMOWITZ, M. and STEGUN, I.A. (1972) Handbook of Mathematical Functions, (Dover, New York).

ALIKAEV, V.V. and PARAIL, V.V. (1984) [In:] International Symposium on Heating in Toroidal Plasmas, 4, 1984-03-21, Roma, vol. 2, 753.

BARANOV, Y.F., BOGDANOVA, N.E., BULYGINSKIJ, D.G., GUSEV, V.K., LARIONOV, M.M., LEVIN, L.S., RAZDOBARIN, G.T. and FEDOROV, V.I. (1983) [In:] International Conference on Plasma Physics and Controlled Nuclear Fusion, 9, 1982-09-01, Baltimore, vol. 2, 125.

BATCHELOR, D.B., GOLDFINGER, R.C. and WEITZNER, H. (1980) IEEE Trans. Plasma Sci., PS-8, 78.

BERNABEI, S. et.al. (1982) Phys. Rev. Lett., 49, 1255.

BEYER, J.B., AUDENAERDE, K. and SCHARER, J.E (1983) IEEE trans. Plasma Sci., PS-11, 255.

BORNATICI, M. (1982) Plasma Phys., 24, 629.

BORNATICI, M., CANO, R., DE BARBIERI, O. and ENGELMANN, F. (1983) Nucl. Fusion, 23, 1153.

BORNATICI, M. and ENGELMANN, F. (1983) Comments Plasma Phys. Controlled Fusion, 8, 57.

BRANDSTATTER, J.J. (1963) An Introduction to Waves, Rays and Radiation in Plasma Media, (McGraw-Hill, New York) 410.

BUDDEN, K.G. and TERRY, P.D. (1971) Proc. R. Soc. London. A., 321, 275.

CONNOR, K.A. (1980) IEEE Trans. Plasma Sci., PS-8, 96.

DE CHAMBRIER, A. (1984) [In:] International Symposium on Heating in Toroidal Plasmas, 4, 1984-03-21, Roma, vol. 1, 137.

DE LUCA, F. and MAROLI, C. (1978) J. Plasma Phys., 20, 299.

ENGELMANN, F. (1984) [In:] International Symposium on Heating in Toroidal Plasmas, 4, 1984-03-21, Roma, vol. 2, 1408.

FESTEAU-BARRIOZ, M.C. et.al. (1984) [In:] International Symposium on Heating in Toroidal Plasmas, 4, 1984-03-21, vol. 2, 1437.

FISCH, N.J. and BOOZER, A.H. (1980) Phys. Rev. Lett., 45, 720.

FRIED, B.D. and CONTE, S.D. (1961) The Plasma Dispersion Function, (Academic Press, New York), 419 p.

HANSEN, F.R., LYNOV, J.P. and MICHELSEN, P. (1984) [In:] International Conference on Plasma Physics, 1984-06-27, Lausanne, vol. 2, 342.

HANSEN, F.R., LYNOV, J.P., MAROLI, C. and PETRILLO, V. (1986). To be published.

HSU, J.Y., CHAN, V.S. and MCCLAIN, F.W. (1983) Phys. Fluids, 26, 3300.

HSUAN, H. et.al. (1984) [In:] International Symposium on Heating in Toroidal Plasmas, 4, 1984-03-21, Roma, vol. 2, 809.

HUI, B., OTT, E., BONOLI, P.T. and GUZDAR, P.N. (1981) Nucl. Fusion, 21, 339.

JORY, H. (1984) [In:] International Symposium on Heating in Toroidal Plasmas, 4, 1984-03-21, Roma, vol. 2, 1424.

MAEKAWA, T., TANAKA, S., TERUMICHI, Y. and HAMADA, Y. (1978) Phys. Rev. Lett., 40, 1379.

MAEKAWA, T., TANAKA, S., TERUMICHI, Y. and HAMADA, Y. (1980) J. Phys. Soc. Jpn., 48, 247.

MCDERMOTT, F.S., BEKEFI, G., HACKETT, K.E., LEVINE, J.S. and PORKOLAB, M. (1982) Phys. Fluids, 25, 1488.

MOELLER, C.P., CHAN, V.S., LA HAYE, R.J. and PRATER, R. (1982) Phys. Fluids, 25, 1211.

RIVIERE, A.C. et.al. (1984) [In:] International Symposium on Heating in Toroidal Plasmas, 4, 1984-03-21, Roma, vol. 2, 795.

PRATER, R., EJIMA, S., LIN, S.H., MOELLER, C., HSU, J.Y., MATSUDA, K., STOCKDALE, R. and THE DOUBLET III PHYSICS AND OPERATIONS GROUPS (1984) [In:] International Symposium Heating in Toroidal Plasmas, 4, 1984-03-21, Roma, vol. 2, 763.

PREINHAELTER, J. and KOPECKY, V. (1973) J. Plasma Phys., 10, 1.

PREINHAELTER, J. (1975) Czech. J. Phys., B25, 39.

PURI, S., LEUTERER, F. and TUTTER, M. (1973) J. Plasma Phys., 9, 89.

STIX, T.H. (1962) The Theory of Plasma Waves, (McGraw-Hill, New York) 283 p.

STODIECK, W. et.al. (1981) [In:] Proceedings of the 8th International Conference on Plasma Physics and Controlled Nuclear Fusion Research, Brussels, 1-10 July 1980. Vol. 1, 9.

SURKO, C.M. and SLUSHER, R.E. (1976) Phys. Rev. Lett., 37, 1747.

WEITZNER, H. and BATCHELOR, D.B. (1979) Phys. Fluids, 22, 1355.

WILHELM, R., ERCKMANN, V., JANZEN, G., KASPAREK, W., MÜLLER, G., RÄUCHLE, E., SCHÜLLER, P.G., SCHWÖRER, K., THUMM, M. and W VII-A TEAM (1984) Plasma Phys. Controlled Fusion, 26, 1433.

APPENDIX A

Polarization of O- and X-waves

The expressions describing the electric field polarization of O- and X-waves propagating at an arbitrary angle to the magnetic field in a homogenous plasma are derived. Firstly, the electric field polarization at finite plasma density is found. Secondly, the O- and X-wave polarization at the plasma boundary where the density vanishes, is evaluated. Finally, we find an expression for the O- and X-mode power content in a linearly polarized wave propagating in vacuum.

A.1. O- and X-wave polarization

Referring to a coordinate system where the refractive index vector, $\underline{N}$, lies in the xz-plane and the magnetic field points along the z-direction, the Maxwell equations describing high-frequency plane waves in a homogenous cold plasma can be reduced to

$$\begin{pmatrix} S-N_z^2 & -iD & N_xN_z \\ iD & S-N_x^2-N_z^2 & 0 \\ N_xN_z & 0 & P-N_x^2 \end{pmatrix} \cdot \begin{pmatrix} E_x \\ E_y \\ E_z \end{pmatrix} = \begin{pmatrix} 0 \\ 0 \\ 0 \end{pmatrix} \tag{A1}$$

where

$$S = 1-X/(1-Y^2)$$

$$D = -XY/(1-Y^2) \tag{A2}$$

$$P = 1-X$$

From the second and the third equation in (A1) we obtain two relations between the components in the electric field vector. By using the expressions in Eqs. (A2) the relations may be written

$$i\frac{E_x}{E_y} = \frac{1}{Y}\left[(1-Y^2)\frac{1-N^2}{X} - 1\right]$$

$$\frac{E_x}{E_z} = \frac{1-X-N^2\sin^2\theta}{N^2\cos\theta\sin\theta} \qquad \text{(A3)}$$

Equations (A3) with N_x and N_z satisfying the Appleton-Hartree dispersion relation (1) describe the polarization of the O- and X-waves.

In order to investigate the wave polarization at the plasma boundary we let $X = 0$ and $N^2 = 1$ in Eqs. (A3). This requires an expression for $(1-N^2)/X$ valid for $X = 0$. An expression for $(1-N^2)/X$ valid for all X, including $X = 0$, is immediately obtained from the Appleton-Hartree dispersion relation (1). By inserting this into the first equation in (A3) we get

$$i\frac{E_x}{E_y} = \frac{2(1-X)}{2(1-X)-Y^2\sin^2\theta \pm \Gamma}\,\frac{1-Y^2}{Y} - \frac{1}{Y} \qquad \text{(A4)}$$

As usual, θ is the angle between the wave vector and the magnetic field.

To investigate the polarization at the plasma boundary, let $X = 0$ in the Eq. (A4) and the second equation in (A3). This leads to the following relations

$$i\frac{E_x}{E_y} = -\frac{Y\sin^2\theta \pm \sqrt{Y^2\sin^4\theta + 4\cos^2\theta}}{2}$$

$$\frac{E_x}{E_z} = -\cot\theta \qquad \text{(A5)}$$

which fully describe the polarization of the two modes in vacuum.

Now consider a plane electromagnetic wave incident from vacuum upon the plasma boundary at an angle θ, as shown in Fig. 28.

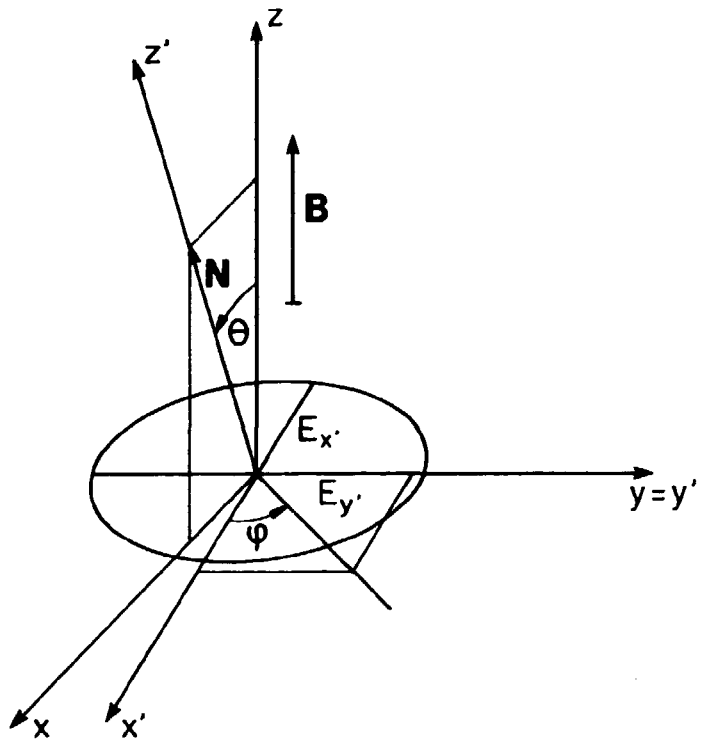

Fig. 28. The coordinate system used for the calculations of the polarization of the electric field at the plasma boundary.

It may be deduced from Eq. (A5) that the incident wave must be elliptically polarized as

$$E_{x'}(t) = RE_o\cos(\omega t)$$

$$E_{y'}(t) = E_o\sin(\omega t)$$

to excite either of the two modes. The ratio, R, of the x'-axis to the y'-axis in the polarization ellipse (see Fig. 28) is given by

$$R_{O,X} = \left|\frac{E_{x'}}{E_{y'}}\right| = \frac{\mp Y\sin^2\theta + \sqrt{Y^2\sin^4\theta + 4\cos^2\theta}}{2\cos\theta} \qquad \text{(A6)}$$

where the upper sign as usually denotes the O-mode.

It is easily shown that the product $R_O R_X = 1$, independent of θ and Y. This indicates that if an elliptically polarized wave excites one mode only, an elliptically polarized wave with the inverse axis ratio excites the other mode only.

A.2. O- and X-mode power content in a linearly polarized wave propagating in vacuum

Consider a linearly polarized wave of the form

$$E_{x'}(t) = E_O\cos\phi\cos(\omega t)$$
$$E_{y'}(t) = E_O\sin\phi\cos(\omega t) \qquad \text{(A7)}$$

propagating in vacuum and incident upon a plasma boundary (see Fig. 28). This wave can be decomposed into two opposite rotating elliptically polarized waves of the form

$$E_{x'}(t) = R_O E_O\cos(\omega t+\phi_O)$$
$$E_{y'}(t) = E_O\sin(\omega t+\phi_O)$$

and

$$E_{x'}(t) = R_X E_X\cos(-\omega t+\phi_X)$$
$$E_{y'}(t) = E_X\sin(-\omega t+\phi_X)$$

The first wave is the ordinary one and the second the extraordinary. By adding the O- and X-wave components of the electric

field vector and equating the result: to Eqs. (A7), we find that E_O, E_X, ϕ_O and ϕ_X must satisfy

$$E_O = E_o \frac{\sqrt{R_O^2\cos^2\phi + \sin^2\phi}}{1 + R_O^2}$$

$$E_X = E_o \frac{\sqrt{R_X^2\cos^2\phi + \sin^2\phi}}{1 + R_X^2}$$

$$\cos\phi_O = \frac{R_O\cos\phi}{\sqrt{R_O^2\cos^2\phi + \sin^2\phi}}$$

$$\cos\phi_X = \frac{R_X\cos\phi}{\sqrt{R_X^2\cos^2\phi + \sin^2\phi}}$$

Finally, the O- and X-mode power content in the incident wave may be determined. Since the power content in each mode is proportional to $\langle E_x^2, \rangle + \langle E_y^2, \rangle$ (the brackets denote time averaging), we find that the ratio, η_O, of the O-mode power content to the total power content in the incident wave is given by

$$\eta_O = \frac{1 + R_O^2\cot^2\phi}{(1+R_O^2)(1+\cot^2\phi)} \qquad (A9)$$

An expression for the relative X-mode power content in the same wave may be obtained by replacing R_O by R_X in Eq. (A9), or alternatively, subtract η_O from 1.

APPENDIX B

A general method for solving the ray equations in Cartesian coordinates

The ray equations

$$\frac{d\underline{r}}{dt} = -\frac{\partial D}{\partial \underline{k}} \Big/ \frac{\partial D}{\partial \omega}$$

$$\frac{d\underline{k}}{dt} = \frac{\partial D}{\partial \underline{r}} \Big/ \frac{\partial D}{\partial \omega} \qquad \text{(B1)}$$

consist of six first-order, ordinary, coupled differential equations. The ray equations may be solved numerically by standard techniques, which require computations of the right-hand sides of Eqs. (B1). A general method to solve the ray equations in Cartesian coordinates is outlined in this appendix. The method presupposes that both the plasma equilibrium and the gradients of the equilibrium are expressed in the rectangular Cartesian coordinates. The method is based on a transformation of the derivatives of the dispersion function, which are first found in a local coordinate system following the ray.

Firstly, it is demonstrated how the derivatives of the dispersion function are transformed from the local to the global coordinate system; secondly, the derivatives of the Appleton-Hartree dispersion function and the hot dispersion function in the local coordinate system are derived.

B.1. Transformation of the derivatives

In the global Cartesian coordinate system in which Eqs. (B1) are solved, the dispersion function is a function of nine variables

$$D = D(\omega_{pe}(\underline{r}),\underline{\omega}_{ce}(\underline{r}),T_e(\underline{r}),\underline{k},\omega)$$

For our purpose it is convenient to introduce the normalized quantities $X = \omega_{pe}^2/\omega^2$, $\underline{Y} = \underline{\omega}_{ce}/\omega$, $Y = (\kappa T_e/m_e c^2)^{1/2}$ and $\underline{N} = c\underline{k}/\omega$, and D may be written

$$D = D(X(\underline{r},\omega),Y(\underline{r},\omega),Y(\underline{r}),\underline{N}(\underline{k},\omega)) \tag{B2}$$

D is of course independent of the choice of coordinate system, and we introduce a local Cartesian coordinate system following the ray. This coordinate system is defined in such a way that the magnetic field lines point along $\hat{z}$, and the refractive index vector lies in the right half-plane of the xz-plane. In the local coordinate system D is a function of five variables

$$D = D(X,Y,Y,N_X,N_Z) \tag{B3}$$

where

$$\begin{aligned} Y(\underline{Y}(\underline{r},\omega)) &= |\underline{Y}| \\ N_Z(\underline{Y}(\underline{r},\omega),\underline{N}(\underline{k},\omega)) &= \underline{N}\cdot(\underline{Y}/Y) \\ N_X(\underline{Y}(\underline{r},\omega),\underline{N}(\underline{k},\omega)) &= (N^2 - N_Z^2)^{1/2} \end{aligned} \tag{B4}$$

For reasons of clarity the functional dependence of $\underline{N}$, $\underline{Y}$, $\underline{r}$, $\underline{k}$ and ω has been stated explicitly in Eqs. (B2) and (B4).

We may now proceed and determine the right-hand sides of the ray equations. By application of the chain rule for differentiation we get from Eq. (B3) that

$$\frac{\partial D}{\partial \underline{N}} = \frac{\partial D}{\partial N_X}\frac{\partial N_X}{\partial \underline{N}} + \frac{\partial D}{\partial N_Z}\frac{\partial N_Z}{\partial \underline{N}} \tag{B5}$$

In the same manner an expression for $\partial D/\partial \underline{r}$ is obtained

$$\frac{\partial D}{\partial \underline{r}} = \frac{\partial D}{\partial X}\frac{\partial X}{\partial \underline{r}} + \frac{\partial D}{\partial Y}\frac{\partial Y}{\partial \underline{r}} + \frac{\partial D}{\partial \gamma}\frac{\partial \gamma}{\partial \underline{r}} + \frac{\partial D}{\partial N_X}\frac{\partial N_X}{\partial \underline{r}} + \frac{\partial D}{\partial N_Z}\frac{\partial N_Z}{\partial \underline{r}} \tag{B6}$$

and $\partial D/\partial \omega$ is given by

$$\frac{\partial D}{\partial \omega} = \frac{\partial D}{\partial X}\frac{\partial X}{\partial \omega} + \frac{\partial D}{\partial Y}\frac{\partial Y}{\partial \omega} + \frac{\partial D}{\partial N_X}\frac{\partial N_X}{\partial \omega} + \frac{\partial D}{\partial N_Z}\frac{\partial N_Z}{\partial \omega}$$

Since $X = \omega_{pe}^2/\omega^2$, $Y = \omega_{ce}/\omega$ and $\underline{N} = c\underline{k}/\omega$ we may rewrite the last equation

$$\frac{\partial D}{\partial \omega} = -\frac{1}{\omega}\left(2X\frac{\partial D}{\partial X} + Y\frac{\partial D}{\partial Y} + N_X\frac{\partial D}{\partial N_X} + N_Z\frac{\partial D}{\partial N_Z}\right) \tag{B7}$$

It is seen that Eqs. (B5) and (B6) together with Eq. (B7) may be combined to form the right-hand sides of the ray equations.

The derivatives of Y, N_X, and N_Z with respect to $\underline{r}$ and $\underline{N}$, appearing in Eqs. (B5) and (B7), are determined from Eqs. (B4). We find that

$$\frac{\partial N_Z}{\partial \underline{N}} = \frac{\underline{Y}}{Y}$$

$$\frac{\partial N_X}{\partial \underline{N}} = \frac{\underline{N} - N_Z\underline{Y}/Y}{N_X}$$

$$\frac{\partial Y}{\partial \underline{r}} = \frac{\underline{Y}}{Y} \cdot \nabla Y$$

$$\frac{\partial N_z}{\partial \underline{r}} = \frac{N_x}{Y} \frac{\partial N_x}{\partial \underline{N}} \cdot \nabla \underline{Y}$$

$$\frac{\partial N_x}{\partial \underline{r}} = - \frac{N_z}{N_x} \frac{\partial N_z}{\partial \underline{r}} \qquad \text{(B8)}$$

$$\frac{\partial X}{\partial \underline{r}} = \nabla X$$

$$\frac{\partial \gamma}{\partial \underline{r}} = \nabla \gamma$$

Equations (B8) represent the transformation of the derivatives of the dispersion function from the local to the global coordinate system. Obviously, Eqs. (B8) are independent of D in the sense that D does not explicitly enter the equations. To make the transformations one needs knowledge only of the plasma equilibrium, the gradients of the equilibrium and the actual value of $\underline{N}$ along the ray trajectory, as determined by Eqs. (B1).

To complete the formation of the ray equations, we need to calculate the derivatives of the dispersion functions with respect to X, Y, γ, N_x and N_z. Instead of evaluating the various derivatives one by one, we find the derivatives of the dispersion functions with respect to a general variable, u, which may be replaced by any of the five above-mentioned variables. This procedure is especially advantageous in the case of the hot dispersion function. However, we start with the cold dispersion function.

B.2. The derivatives of the Appleton-Hartree dispersion function

We introduce a variable selection function, H, defined as

$$H(u,u') = \begin{cases} 1 & \text{for } u = u' \\ 0 & \text{for } u \neq u' \end{cases}$$

The derivative of the cold dispersion function with respect to u, is found by straightforward differentiation of Eq. (18). We find that

$$\frac{\partial D}{\partial u} = -2\left[N_X H(u,N_X) + N_Z(u,N_Z) + \frac{(1-2X)Q\partial X/\partial u - X(1-X)\partial Q/\partial u}{Q^2}\right]$$

where

$$Q = 2(1-X) - Y^2\sin^2\theta \pm \Gamma$$

$$\frac{\partial Q}{\partial u} = -\left[2H(u,X) + 2Y\sin^2\theta H(u,Y) + Y^2\frac{\partial \sin^2\theta}{\partial u} \mp \frac{\partial \Gamma}{\partial u}\right]$$

$$\frac{\partial \sin^2\theta}{\partial u} = \frac{2N_X N_Z\left[N_Z H(u,N_X) - N_X H(u,N_Z)\right]}{N^4}$$

$$\frac{\partial \Gamma}{\partial u} = \left\{2Y^3\sin^4\theta H(u,Y) + Y^4\sin^2\theta\frac{\partial \sin^2\theta}{\partial u} + 2Y(1-X)\left[2\cos^2\theta H(u,Y) - Y(2\cos^2\theta H(u,Y) + (1-X)\frac{\partial \sin^2\theta}{\partial u}\right)\right]\right\}/\Gamma$$

B.3. The derivatives of the hot dispersion function

As in the case of the cold dispersion function, we differentiate the hot dispersion function with respect to a general variable, u. From Eq. (21) we get

$$\frac{\partial D}{\partial u} = N_x^4\frac{\partial A}{\partial u} + 4N_x^3 AH(u,N_x) + N_x^2\frac{\partial B}{\partial u} + 2N_x BH(u,N_x) + \frac{\partial C}{\partial u}$$

where A, B and C are defined in Eqs. (22). By differentiation of the expressions for A, B and C, we get

$$\frac{\partial A}{\partial u} = 2\left[N_z\frac{\partial C_{xz}}{\partial u} + C_{xz}H(u,N_z)\right] + \frac{\partial K_{xx}}{\partial u} + 2C_{xz}\frac{\partial C_{xz}}{\partial u}$$

$$\frac{\partial B}{\partial u} = 2\left[N_z^3\frac{\partial C_{xz}}{\partial u} + 3N_z^2 C_{xz}H(u,N_z)\right]$$

$$+ \left(\frac{\partial K_{xx}}{\partial u} + \frac{\partial K_{zz}}{\partial u} + 2C_{yz}\frac{\partial C_{yz}}{\partial u} + 2C_{xz}\frac{\partial C_{xz}}{\partial u}\right)N_z^2$$

$$+ 2N_z(K_{xx} + K_{zz} + C_{yz}^2 + C_{xz}^2)H(u,N_z)$$

$$- 2\left(C_{xy}\frac{\partial C_{yz}}{\partial u} + C_{yz}\frac{\partial C_{xy}}{\partial u} + K_{yy}\frac{\partial C_{xz}}{\partial u} + C_{xz}\frac{\partial K_{yy}}{\partial u}\right)N_z$$

$$- 2(C_{xy}C_{yz} + K_{yy}C_{xz})H(u,N_z)$$

$$- K_{xx}\left(\frac{\partial K_{yy}}{\partial u} + \frac{\partial K_{zz}}{\partial u}\right) - (K_{yy} + K_{zz})\frac{\partial K_{xx}}{\partial u}$$

$$+ 2C_{xy}\frac{\partial C_{xy}}{\partial u} - 2K_{xx}C_{yz}\frac{\partial C_{yz}}{\partial u} - C_{yz}^2\frac{\partial K_{xx}}{\partial u}$$

$$- 2(C_{xz}C_{yz}\frac{\partial C_{xy}}{\partial u} + C_{xz}C_{xy}\frac{\partial C_{yz}}{\partial u} + C_{yz}C_{xy}\frac{\partial C_{xz}}{\partial u})$$

$$- C_{xz}^2\frac{\partial K_{yy}}{\partial u} - 2C_{xz}K_{yy}\frac{\partial C_{xz}}{\partial u}$$

$$\frac{\partial C}{\partial u} = \frac{C}{K_{zz}}\frac{\partial K_{zz}}{\partial u}$$

$$+ K_{zz}[4N_z^3H(u,N_z) - 2N_z(K_{xx} + K_{yy})H(u,N_z)$$

$$- N_z^2(\frac{\partial K_{xx}}{\partial u} + \frac{\partial K_{yy}}{\partial u}) + K_{xx}\frac{\partial K_{yy}}{\partial u} + K_{yy}\frac{\partial K_{xx}}{\partial u} - 2C_{xy}\frac{\partial K_{xy}}{\partial u}]$$

From Eqs. (23) we compute the following derivaties appearing in the expressions listed above.

$$\frac{\partial K_{xx}}{\partial u} = \frac{1}{B_{xx}}\frac{\partial B_{xx}}{\partial u}(K_{xx}-1)$$

$$+ B_{xx}\sum_{n=0}^{\infty}{}'n^2[\frac{\partial \lambda}{\partial u}I_n'(\lambda)\{Z(\zeta_n) + Z(\zeta_{-n})\}$$

$$+ I_n(\lambda)\{\frac{\partial \zeta_n}{\partial u}Z'(\zeta_n) + \frac{\partial \zeta_{-n}}{\partial u}Z'(\zeta_{-n})\}]$$

$$\frac{\partial C_{xy}}{\partial u} = \frac{1}{B_{xy}}\frac{\partial B_{xy}}{\partial u}C_{xy}$$

$$- B_{xy}\sum_{n=0}^{\infty}{}'n[\frac{\partial \lambda}{\partial u}\{I_n'(\lambda) - I_n''(\lambda)\}\{Z(\zeta_n) - Z(\zeta_{-n})\}$$

$$+ \{\frac{\partial \zeta_n}{\partial u}Z'(\zeta_n) - \frac{\partial \zeta_{-n}}{\partial u}Z'(\zeta_{-n})\}\{I_n(\lambda) - I_n'(\lambda)\}]$$

$$\frac{\partial C_{xz}}{\partial u} = \frac{1}{B_{xz}} \frac{\partial B_{xz}}{\partial u} C_{xz}$$

$$- B_{xz} \sum_{n=0}^{\infty}{}' n\Big[\frac{\partial \lambda}{\partial u} I'(\lambda)\{-Z'(\zeta_n) + Z'(\zeta_{-n})\}$$

$$+ I_n(\lambda)\{-\frac{\partial \zeta_n}{\partial u} Z''(\zeta_n) + \frac{\partial \zeta_{-n}}{\partial u} Z''(\zeta_{-n})\}\Big]/2$$

$$\frac{\partial K_{yy}}{\partial u} = \frac{1}{B_{yy}} \frac{\partial B_{yy}}{\partial u}(K_{yy}-1)$$

$$+ B_{yy} \sum_{n=0}^{\infty}{}' \frac{\partial \lambda}{\partial u}\Big[n^2 I_n'(\lambda) + 4\lambda\{I_n(\lambda) - I_n'(\lambda)\}$$

$$+ 2\lambda^2\{I_n'(\lambda) - I_n''(\lambda)\}\{Z(\zeta_n) + Z(\zeta_{-n})\}\Big]$$

$$+ \Big[\frac{\partial \zeta_n}{\partial u} Z'(\zeta_n) + \frac{\partial \zeta_{-n}}{\partial u} Z'(\zeta_{-n})\Big]\Big[n^2 I_n(\lambda)$$

$$+ 2\lambda^2\{I_n(\lambda) - I'(\lambda)\}\Big]$$

$$\frac{\partial C_{yz}}{\partial u} = \frac{1}{B_{yz}} \frac{\partial B_{yz}}{\partial u} C_{yz}$$

$$- B_{yz} \sum_{n=0}^{\infty}{}' \frac{\partial \lambda}{\partial u}\Big[I_n'(\lambda) - I_n''(\lambda)\Big]\Big[\zeta_n Z(\zeta_n) + \zeta_{-n} Z(\zeta_{-n})\Big]$$

$$+ \Big[I_n(\lambda) - I_n'(\lambda)\Big]\Big[\frac{\partial \zeta_n}{\partial u}\{Z(\zeta_n) + \zeta_n Z'(\zeta_n)\}$$

$$+ \frac{\partial \zeta_{-n}}{\partial u}\{Z(\zeta_{-n}) + \zeta_{-n} Z'(\zeta_{-n})\}\Big]$$

$$\frac{\partial K_{zz}}{\partial u} = \frac{1}{B_{zz}} \frac{\partial B_{zz}}{\partial u}(K_{zz}-1)$$

$$- B_{zz} \sum_{n=0}^{\infty}{}' \frac{\partial \lambda}{\partial u} I_n'(\lambda) \left[\zeta_n Z'(\zeta_n) + \zeta_{-n} Z'(\zeta_{-n})\right]$$

$$+ I_n(\lambda)\left[\frac{\partial \zeta_n}{\partial u}\{Z'(\zeta_n) + \zeta_n Z''(\zeta_n)\}\right.$$

$$\left. + \frac{\partial \zeta_{-n}}{\partial u}\{Z'(\zeta_{-n}) + \zeta_{-n} Z''(\zeta_{-n})\}\right]$$

From Eqs. (24) we get

$$\frac{1}{B_{xx}} \frac{\partial B_{xx}}{\partial u} = \frac{1}{X} H(u,X) + \frac{1}{\zeta_o} \frac{\partial \zeta_o}{\partial u} - \frac{\partial \lambda}{\partial u} - \frac{1}{\lambda} \frac{\partial \lambda}{\partial u}$$

$$\frac{1}{B_{xy}} \frac{\partial B_{xy}}{\partial u} = \frac{1}{X} H(u,X) + \frac{1}{\zeta_o} \frac{\partial \zeta_o}{\partial u} - \frac{\partial \lambda}{\partial u}$$

$$\frac{1}{B_{xz}} \frac{\partial B_{xz}}{\partial u} = \frac{1}{X} H(u,X) - \frac{\partial \lambda}{\partial u} - \frac{1}{Y} H(u,Y) - \frac{1}{N_z} H(u,N_z) - \frac{1}{\lambda} \frac{\partial \lambda}{\partial u}$$

$$\frac{1}{B_{yy}} \frac{\partial B_{yy}}{\partial u} = \frac{1}{B_{xx}} \frac{\partial B_{xx}}{\partial u}$$

$$\frac{1}{B_{yz}} \frac{\partial B_{yz}}{\partial u} = \frac{1}{X} H(u,X) - \frac{\partial \lambda}{\partial u} - \frac{1}{Y} H(u,Y) - \frac{1}{N_z} H(u,N_z)$$

$$\frac{1}{B_{zz}} \frac{\partial B_{zz}}{\partial u} = \frac{1}{B_{xy}} \frac{\partial B_{xy}}{\partial u}$$

and, finally, we determine $\partial\lambda/\partial u$ and $\partial\zeta_n/\partial u$ from Eqs. (25) and (26).

$$\frac{\partial\lambda}{\partial u} = 2\lambda\left[\frac{1}{N_X}H(u,N_X) + \frac{1}{\gamma}H(u,\gamma) - \frac{1}{Y}H(u,Y)\right]$$

$$\frac{\partial\zeta_n}{\partial u} = \zeta_n\left[\frac{n}{1+nY}H(u,Y) - \frac{1}{N_Z}H(u,N_Z) - \frac{1}{\gamma}H(u,\gamma)\right]$$

Risø National Laboratory **Risø – M – 2594**

ELECTRON CYCLOTRON RESONANCE HEATING OF A HIGH-DENSITY PLASMA

Flemming Ramskov Hansen

Date 31 July 1986

Department or group: Physics

Groups own registration number(s):

Project/contract no.:

Pages 88 Tables 1 Illustrations 28 References 38

ISBN 87-550-1243-4

Abstract (Max. 2000 char.)

Various schemes for electron cyclotron resonance heating of tokamak plasmas with the ratio of electron plasma frequency to electron cyclotron frequency, ω_{pe}/ω_{ce}, larger than 1 on axis, are investigated. In particular, a mode conversion scheme is investigated using ordinary waves at the fundamental of the electron cyclotron frequency. These are injected obliquely from the outside outside of the tokamak near an optimal angle to the magnetic field lines. This method involves two mode conversions. The ordinary waves are converted into extraordinary waves near the plasma cut-off layer. The extraordinary waves are subsequently converted into electrostatic electron Bernstein waves at the upper hybrid resonance layer, and the Bernstein waves are completely absorbed close to the plasma centre. Results are presented from ray-tracing calculations in full three-dimensional geometry using the dispersion function for a hot non-relativistic plasma. Radial profiles for the power deposition and the non-inductive wavedriven current due to the Bernstein waves are calculated for realistic antenna radiation patterns with parameters corresponding to the Danish tokamak DANTE and to Princeton's PLT.

Descriptors

Available on request from Risø Library, Risø National Laboratory, (Risø Bibliotek, Forskningscenter Risø).
P.O. Box 49, DK-4000 Roskilde, Denmark.
Telephone 02 37 12 12, ext. 2262. Telex: 43116, Telefax: 02 36 06 09

RR 86000 99